Master Thesis Project

Thermal oxidation of ruthenium silicide compounds

Abhijay Khatri

Examiner and supervisor: Dr. Roland Bliem

Daily Supervisor: Stefan van Vliet

Second Reviewer: Prof. Dr. Paul Planken

MSc Physics & Astronomy: Advanced Matter and Energy Physics

2022-2024

Universiteit van Amsterdam

ARCNL

UNIVERSITEIT VAN AMSTERDAM

Abstract

Ruthenium silicide compounds are a class of interesting semiconducting materials that have shown promise as oxidation-resistant coatings in modern electronics. Gaining insights into the oxidation mechanism of ruthenium silicide compounds is relevant for determining if ruthenium silicide compounds may be used for developing oxidation–resistant coatings. This work investigates the formation and subsequent thermal oxidation of ruthenium silicide compounds. The formation of silicide compounds upon UHV annealing of PLD–deposited Ru on Si(100) substrates is followed using in-situ XPS. Results obtained show that under similar deposition and annealing conditions, different silicide compounds are formed at the sample's surface and a new unidentified peak is observable. The formation of different Ru_xSi_y phases is characterized using their composition and changes in the shape and position of the plasmon-loss peak feature. The thermal oxidation of ruthenium silicide compounds at 350°C and 700°C showed that the ruthenium in ruthenium silicide compounds is extremely resistant to oxidation when Ru_2Si_3 is the dominant phase. However, when the dominant phase is approximately an equiatomic Ru_xSi_y compound, thermal oxidation at 550°C causes ruthenium to oxidize, thereby resulting in the formation of rutile ruthenium oxide.

Keywords: Ruthenium silicide, X-ray photoelectron spectroscopy, surface oxidation, Pulsed-laser deposition, Plasmon loss satellites

Contents

Acknowledgments

I would like to thank ARCNL for providing me with the unique opportunity to intern within the Materials and Surface Science (MatSurf) for EUV lithography group. ARCNL provided me with the wonderful opportunity to do research in the field of Surface Science along with an exceptional and start of the art experimental environment. I believe ARCNL is distinguished research-institute through which I was able to learn vastly during the internship. I would further like to thank the entire MatSurf group for their constant support throughout the internship. Finally, I would specifically like to thank the following people without whom this project would not have been possible:

Dr. Roland Bliem (group leader MatSurf, thesis supervisor)

For many thought-provoking discussions, guidance, and support throughout this project.

Stefan van Vliet (PhD candidate MatSurf)

For their excellent supervision as my daily supervisor and for helping me develop analytical and experimental skills relevant to laser and vacuum physics, and for helping me perform and conduct XPS experiments.

List of Abbreviations

m – meters

nm – Nanometers (10^{-9} m)

NUP – New unidentified peak

XPS – X-ray photoelectron spectroscopy

UHV – Ultra-high vacuum

NAP – Near-ambient pressure

PL – Plasmon loss

Hz – Hertz

eV – Electron volt

KE – Kinetic energy

BE – Binding energy

PLD – Pulsed laser deposition

mbar – Millibar (10^{-3} bar)

J – Joules

cm – Centimeters (10^{-2} m)

mm – Millimeters (10^{-3} m)

kV – Kilovolt (10^{3} Volts)

NA – Not applicable

ºC – Degree Celcius

mA - Milliampere

1. Introduction

The evolution of technology has required the exploration and use of novel materials which have in turn enabled the existence of modern technology and electronics used by more than seven billion people today. One class of novel materials that enabled this modern technological revolution is metal silicides. Although metal silicide compounds have been known to exist since the 19th century, they became extremely important in the late 20th century and 21st century for enabling the advancement of modern technology. In recent years, some metal silicide compounds like $TiSi_2$, PtSi, Pd_2Si, $MoSi_2$, WSi_2, and $TaSi_2$, have become essential for developing modern electronic circuits like CMOS (Complementary Metal-Oxide Semiconductor) technology, VLSI (Very Large-Scale Integration) technology [1]. Metal silicides like PtSi have also been used to develop semiconductor nanowires for the emerging technology of optoelectronics [2]. These metal silicides are characterized as narrow bandgap semiconductors (smaller bandgap than that of silicon) and their use in VLSI and CMOS technologies is attributed to their low specific resistivity, high oxidation resistance, low contact resistance to silicon, and high melting point [1-2].

Recently, another narrow bandgap metal silicide, Ru2Si3, has become important for developing advanced CMOS technology [3], infrared detectors [4], thermoelectric applications [5], diffusion barriers [6], and light-emitting diodes [7]. Ruthenium is known to form stable silicides while favoring the formation of Ru2Si3 in the presence of an abundance of silicon [12]. The formation of different ruthenium silicide compounds using different techniques such as arc-melting [14], pulsed laser deposition [13], and physical vapor deposition [15] have already been studied and reported. Although ruthenium silicide films have properties comparable to other silicides [12], the use of ruthenium silicide thin-films so far has only been experimental. The interest in ruthenium silicide compounds arises from the need to find alternatives to ruthenium thin-films that are used regularly in electronics [8], semiconductors [9], and aerospace industries [11]. The need arises because ruthenium thin-films have been known to oxidize and form rutile-ruthenium dioxide [16]. On the other hand, previous studies on the oxidation of ruthenium silicide compounds have shown that the ruthenium in certain ruthenium silicide compounds does not oxidize under high oxygen pressures and high temperatures [19]. Instead, the oxidation of ruthenium silicide compounds only results in the oxidation of silicon, forming a SiO_x layer on top of the ruthenium silicide compound [12, 19, 20].

Recent studies on the formation of ruthenium silicide compounds have also shown that PLD–deposited ruthenium on Si (100) when annealed at/above 550°C in argon gas [13] results in the formation of Ru_2Si_3 phase as the dominant phase. Recent studies on the oxidation of other silicide films such as TiSi2 have shown that some stable metal silicides tend to oxidize and form metal–oxide structures on top of the metal–silicide compound [17]. Previous studies have also shown that the oxidation of Ru2Si3 at high temperatures and high oxygen pressures does not result in the breakdown of the Ru2Si3 phase and instead results in the formation of SiOx compounds at the surface [19, 21]. However, it is still uncertain if oxidation of different Ru_xSi_y phases like RuSi, oxidize Ru to form metal-oxide structures. Thus, if ruthenium silicide compounds are to be used in the development of modern technology and devices, as oxidation-resistant barrier layers or as contacts in semiconductor devices, it is important to investigate whether the formation of thin-film ruthenium silicide compounds on a Si (100)

substrate and their subsequent oxidation results in the formation of rutile RuO2 or an intermediate layer of Ru-O-Si at the sample's surface.

Therefore, for this study, the synthesis and oxidation of ruthenium silicide compounds are investigated using X-ray photoelectron spectroscopy (XPS). First, using in-situ XPS it is reinvestigated whether the UHV annealing of Ru on Si (100) substrate at 700°C for 80 minutes results in the formation of any other ruthenium silicide phase except the Ru2Si3 phase. Second, the thermal oxidation of different ruthenium silicide phases at different temperatures and oxygen pressures (Table 3) is monitored using in-situ NAP-XPS.

2. Theoretical Background

2.1. Thermal oxidation of ruthenium silicide compounds

Oxidation is defined as a chemical reaction that occurs when a material comes into contact with oxygen or an oxidizing agent [1]. Thermal oxidation is the process through which an oxide layer is produced on the surface of a material at elevated temperatures [2]. Thermal oxidation of thin-film metal-silicide compounds have varying oxidation behavior, and this behavior is dictated by the physical and chemical properties of the metal forming the metal-silicide compound [3].

The formation of ruthenium silicide compounds on a silicon substrate is dictated by the following reaction:

$$xRu + ySi \xrightarrow{UHV\ annealing\ @\ 625℃} Ru_xSi_y \quad (1)$$

Equation (1) states that in the abundance of silicon, ruthenium deposited on top of a Si (100) substrate and thereafter annealed in ultra-high vacuum (UHV) at 625°C for 60 minutes, will result in the production of ruthenium silicide compounds through the mechanism of inter-layer diffusion of silicon atoms [3]. Current research suggests that the ruthenium silicide compound formed at a sample's surface (using the above reaction) is mostly Ru_2Si_3 [2].

This formation of ruthenium silicide compounds happens because, at temperatures above 450°C, it becomes energetically favorable for the silicon atoms to start diffusing toward the deposited ruthenium and convert almost all of the metallic ruthenium to Ru_2Si_3, which is characterized as a semiconductor. The Ru_2Si_3 phase is called a semiconductor because the compound is known to have a bandgap of 0.8 eV at room temperature [4].

Ruthenium and its compounds are widely studied for their application in the semiconductor and lithography industry. Ruthenium oxide is currently used in dynamic random access memory. Previous studies have shown that thermal oxidation of Ru thin-films at temperatures above 600°C results in the formation of rutile ruthenium dioxide [8].

Silicon and its various compounds are credited for the emergence and success of almost all modern electronics that are used today. Therefore, the oxidation of silicon and its compounds has been widely studied for more than half a century. Thermal oxidation of Si (100) substrates between temperatures of 600°C – 900°C results in the formation of a silicon dioxide (SiO_2) layer on top of the Si (100) substrate [9].

As mentioned above, the thermal oxidation of thin-film metal-silicide compounds is dictated by the physical and chemical properties of the metal used to create the metal-silicide compounds. The thermal oxidation of ruthenium silicide compounds is studied because the oxidation behavior of ruthenium silicide is poorly understood. In fact, according to the current hypothesis, the thermal oxidation of ruthenium silicide compounds at 700°C results in the following reaction:

$$Ru_xSi_y + Si(100) + O_2 \xrightarrow{Thermal\ Oxidation\ (O_2)\ @\ 700℃} Ru_xSi_y + SiO_2 \quad (2)$$

Equation (2) above implies that during the thermal oxidation of ruthenium silicide compounds, ruthenium in ruthenium silicide does not undergo oxidation and maintains its stoichiometric ratio. Instead, because of the capability of silicon atoms to diffuse upwards, the silicon atoms diffuse from below the ruthenium silicide layer to form a silicon oxide layer above the surface of the ruthenium silicide layer [5, 6, 10]. However, current data and observations are insufficient to prove that ruthenium in ruthenium silicide does not oxidize at different temperatures and oxygen pressures. Previous studies on the thermal oxidation of ruthenium silicide compounds have also not been able to determine whether pressure or temperature is the limiting factor in the case of the thermal oxidation of Ru_xSi_y compounds.

Another important characteristic of ruthenium is its tendency to form a rutile ruthenium dioxide (RuO_2) layer on top of a polycrystalline or single-crystal ruthenium sample during thermal oxidation of ruthenium at temperatures above 200°C [7]. On the other hand, previous studies have been unable to show whether ruthenium silicide compounds, upon thermal oxidation at temperatures ranging from 400°C – 700°C form a rutile ruthenium dioxide phase along with the formation of silicon dioxide [5, 6, 10].

2.2. X-ray photoelectron spectroscopy

X-ray photoelectron spectroscopy (XPS) is a surface-sensitive analysis technique that uses X-rays to excite core-level electrons. The emitted electrons are called photoelectrons whose measured kinetic energy can be used to probe the chemical state information of the surface of almost any material and element except insulators, hydrogen, and helium [1, 5]. XPS is based on the photoelectric effect, which was discovered by Henrich Hertz in 1887, and was scientifically described by Albert Einstein in 1905 which also earned him a Nobel Prize in physics (1921). However, the XPS analysis technique was developed at the University of Uppsala in Sweden by Kai Siegbahn which earned him a Nobel Prize in physics (1981) [1].

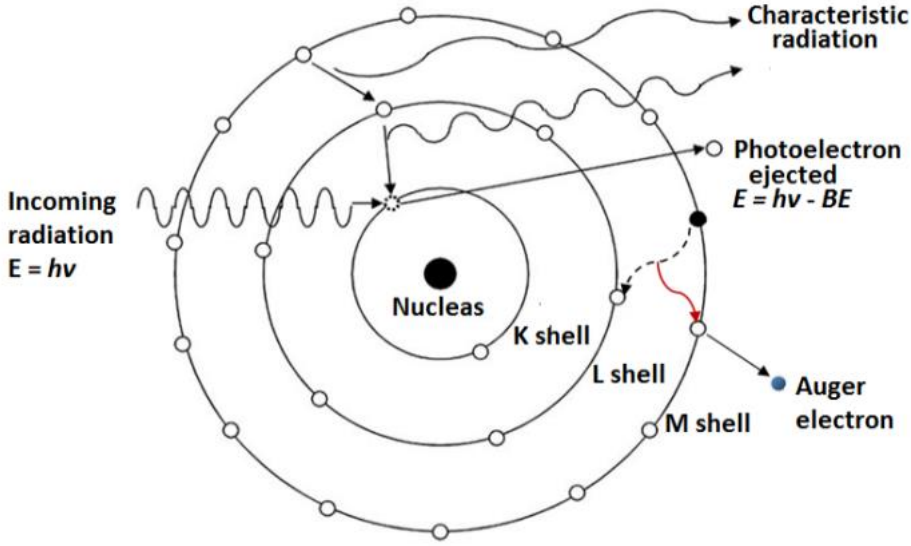

Figure 1: Illustrative diagram of the photoelectric effect [3].

The photoelectric effect described by equation 3 and illustratively shown in Figure 1, is a process where a photon with energy hω excites an electron with an initial binding energy (BE). The excited photoelectron is emitted with a specific kinetic energy (KE) when it

absorbs a photon of energy hω. The generation of photoelectrons from a surface only occurs if the energy of the incoming photon, hω is greater than the BE of the excited photoelectron. In XPS the x-ray radiation used to generate photoelectrons is in the range of 100eV – 10keV. This energy range of X-rays corresponds to probing the core-level electrons of an element [1].

$$h\omega = BE + KE + \Phi_{spec} \quad (3)$$

In equation (3), the 'Φ_{spec}' is the spectrometer work function which is always assumed to be constant and calibrated to a specific analyzer so that the calculated BEs and KEs are also calibrated to Φ_{spec}. The photoelectrons ejected with a certain KE, can be used to calculate the BE of the ejected photoelectron. The BEs of the ejected core hole photoelectrons is characteristic of a particular element and its orbital. Small shifts in the detected KE (or BE) of a photoelectron is indicative of changes in the chemical environment or oxidation state of the constituent elements [1].

The shift in the BE/KE arises because the BE of an electron is dependent on the interaction between the Coulomb attraction of the electron towards the nucleus and the screening of this attraction by the other electrons in the vicinity of that electron. Changing the oxidation state or the chemical environment of the sample changes the number of electrons surrounding an atom. The increase or decrease in the number of electrons surrounding an atom results in changing the amplitude of Coulomb attraction and the screening of the nuclear charge. The above-described effect thereby results in changing the BE of that detected photoelectron. Changes in the oxidation state or chemical environment of a crystalline structure also causes the BE of a photoelectron to decrease due to an electrostatic effect called the Madelung potential [4]. Therefore, XPS is a useful tool in determining and analyzing the sample composition and chemical environment of the constituent elements.

Some additional features of XPS include the emission and detection of Auger electrons or X-ray fluorescence with characteristic energy. During XPS, the core-hole electron which becomes a photoelectron leaves a hole behind when it is ejected from the atom. This creates an ionized state which relaxes and returns to the ground state when a valence electron fills up the core-hole. This relaxation process releases an energy that results in the emission of Auger electrons or x-ray fluorescence with a characteristic energy. These Auger electrons can be detected with XPS and used to characterize additional properties of the material [2].

$$I = I_0 \exp(-d/\lambda) \quad (4)$$

XPS systems allow its users to probe 5-10 nm of the surface of a particular material. The surface sensitivity of the system is determined by calculating the depth (in nm) at which an electron may be generated and thereby escape the surface of the material without undergoing inelastic scattering. The intensity of the photoelectrons emitted at the surface (I) is described by Beer–Lambert's law in equation (4). In this equation, I_0 is the intensity of the photoelectrons emitted at a depth d below the surface and λ is the attenuation length. λ or the inelastic mean free path (IMFP) is defined as the average distance an electron with certain KE travels before it undergoes inelastic scattering. However, the attenuation length is a little different from IMFP because it also takes into consideration the effects of elastic scattering that occur when a photoelectron tries to escape the surface from depth d inside the surface.

The information depth or the sampling depth is defined as the depth from which 95% of all photoelectrons detected are generated. The sampling depth for XPS is equivalent to 3λ [6].

3. Methods

3.1. Experimental Setup

3.1.1. Pulsed Laser Deposition

All samples in the study were created using pulsed-laser deposition (PLD) which is a physical vapor deposition technique and is especially useful for depositing thin films of up to a few micrometers in thickness [10]. The PLD system that is used for this research was developed by TSST (Twente Solid State Technology B.V.). The laser that was used for deposition is developed by Coherent Inc and the laser system is called COMPex 201F. This is a krypton fluoride excimer laser with a wavelength of 248 nm. The PLD system consists of two main components 1. The PLD chamber and 2. The loadlock. The loadlock is used for loading samples inside the PLD chamber and ensures that the PLD chamber is always in UHV conditions. The PLD chamber and the sample inside it are kept in an ultra-high vacuum with a base pressure of 1.2 x 10^{-9} mbar.

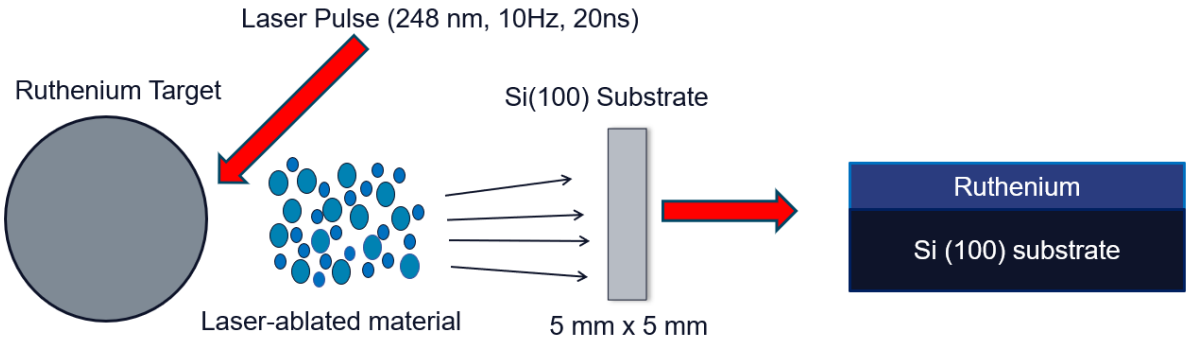

Figure 1: Schematic diagram depicting the PLD process of depositing Ru on top of Si (100) substrate

Parameter	Value	Units
Deposition fluence	8.1	J/cm^2
Laser discharge voltage	20.5	kV
Laser repetition frequency	10	Hz
Ar gas deposition pressure	4.0 x 10^{-2}	mbar
Deposition temperature	Room temperature	°C
Spot Size	0.4	mm^2
Number of deposition pulses	NA	15000

Table 1: PLD operating parameters for depositing 25 nm polycrystalline Ru on a Si (100) substrate.

During PLD, high-energy laser pulses are used to ablate the surface of the solid Ru target which is inside the PLD chamber. The ablated Ru atoms condense on the Si (100) substrate to form a thin layer of polycrystalline ruthenium. The operating conditions for the deposition of 25 nm of ruthenium metal onto a Si (100) substrate with native oxide are described here and displayed in Table 1. The deposition is made at room temperature. The fluence of the laser is 8.1 J/cm^2, the repetition rate is 10 Hz and the pulse duration is 20 ns. A 99.95% pure Ru target (Alineason Materials Technology GmbH) was used for the deposition process and the deposition was carried out at a base pressure of 4 x 10^{-2} mbar of inert gas Argon. This was determined as the best pressure for maximum deposition of Ru atoms on the Si (100) surface. The spot size of the laser on the target was 0.4 mm^2 and the 15000 pulses were used to deposit 25 nm of Ru on the Si (100) substrate.

3.1.2. XPS

The XPS technique is used for conducting this research project. Specifically, the XPS measurements were conducted using a Near Ambient Pressure XPS (NAP-XPS) setup. The X-ray source used for this research employs a monochromatic Al Kα source (hν = 1486.6 eV) operating at a filament current of 2.3 A, emission current of 20 mA, and anode voltage of 13.0 kV. The X-ray source is separated from the measuring chamber by a silicon-nitride window. This separation allows the X-ray source to operate at elevated pressures.

The generation of monochromatic X-rays, depicted in Figure 2, starts by creating a potential gap between the cathode and aluminum anode. The cathode side has a separate low-voltage circuit on the filament which is responsible for generating current. The release of electrons from the filament happens due to the thermionic emission effect. The electrons are accelerated towards the aluminum anode because of the above-mentioned potential gap. Finally, the X-rays are generated and released because of the bombardment of electrons towards the aluminum anode [1]. After X-rays are generated, they are turned into monochromatic X-rays with the required energy using a quartz crystal, which serves as a diffraction grating.

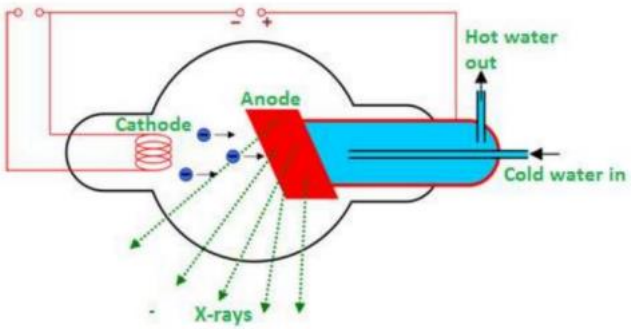

Figure 2: Production of X-rays process [23].

The generated monochromatic X-rays are bombarded onto the sample which is held stable in the measurement chamber. The analyzer cone collects a fraction of the photoelectrons that are ejected from the sample. To analyze the collected photoelectrons, they are directed toward the hemispherical analyzer. The specific analyzer used for this study is the SCIENTA HiPP-3 electron spectrometer, depicted in Figure 3. This analyzer was developed for analyzing XPS

samples in UHV conditions and is also capable of analyzing samples in near-ambient pressure conditions. Therefore, the pressures inside the measurement chamber can vary from mbar to UHV conditions.

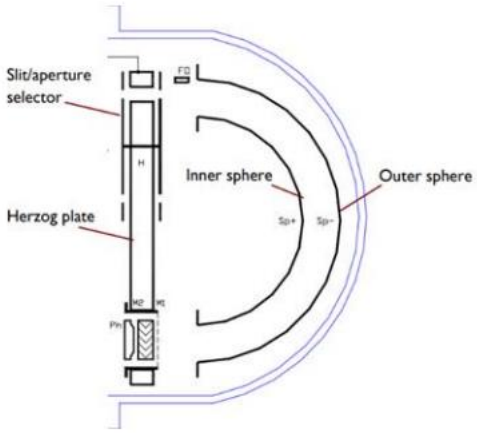

Figure 3: Schematic diagram of the SCIENTA HiPP-3 analyzer from the device manual.

The analyzer only accepts photoelectrons in a fixed energy window, also known as the pass energy. The electrostatic field created between the inner and outer sphere (Figure 3) is used for tuning the energy of the incoming electrons so that the electrons fit in this pass energy window. The SES software (also provided by SCIENTA OMICRON) is used for collecting data from the XPS device. The software creates XPS spectra from the photoelectrons that are in the range of the chosen pass energy.

Additionally, NAP-XPS used for this research, has the feature of gas inflow lines for gas exposures for up to 20 mbar pressures. In this research, we use oxygen gas as the inflow gas at various pressures with a maximum pressure of 5.33 x 10^{-3} mbar.

An Extorr XT Series residual gas analyzer (RGA) is used to monitor the presence of gaseous species/ions in the XPS measurement chamber. This device is only used during the oxidation of the samples and its purpose is to make sure that no unknown species (for example: water, methane, nitrogen, etc.) are present inside the XPS measurement chamber.

3.2. Experimental Approach

3.2.1. Sample Preparation

Ultra-high vacuum systems require careful sample preparation. To study the oxidation of ruthenium silicide compounds, the first step was to create ruthenium silicide compounds using PLD. Before depositing Ru on the Si (100) substrate, the substrate was first cleaned in an ultrasonic bath of acetone followed by an ultrasonic bath of isopropyl alcohol. The Si substrate was mounted on an Inconel 625 sample holder using silver paint (Silberleitlack LS200N BC by Hans Wolbring GmbH). Inconel 625 is a nickel-based superalloy that is resistant to changes caused by heating and oxidation at very high temperatures [2]. The sample was inserted into the loadlock and subsequently transferred to the PLD chamber for deposition of Ru as described in the PLD process above.

After deposition, the sample was transferred to the XPS measurement chamber without breaking the vacuum thereby preventing oxygen and water exposure before annealing the sample. Inside the measurement chamber, Ru deposited Si (100) substrate was annealed to 700°C in UHV with a radiative heater for at least 80 minutes to enable conversion of metallic ruthenium to ruthenium silicide compounds. The surface temperature of the sample was measured using an infrared pyrometer (M311, Sensortherm).

Oxidation of ruthenium silicide was performed at the temperatures and pressure given in the results section (Table 3) below. The temperature was kept constant for each experiment while the pressure was increased approximately every 100 minutes first by x10 and then by x5 to test the oxidation resistance of ruthenium silicide at different temperatures and pressures.

3.2.2. Measurement Procedure using XPS

To perform the experiments, the first step is to switch on the X-ray source. The second step is to modify and fix the position of the sample relative to that of the XPS cone mechanically so that the number of photoelectrons detected is maximized. After finding an optimal position, the desired spectra are recorded using the SES software and consist of a graph where the number of photoelectrons detected (intensity) is recorded as a function of BE (or KE).

First, the overview spectrum of the sample (with a BE range of 1100 – 0 eV) is recorded at pass energy 300 eV. This spectrum is recorded to identify all the elements present at the sample's surface, including any unwanted contaminants like C, O, Ni etc. After identification of the main elements present at the sample's surface, detailed core-level spectrum of the desired atomic species of interest are recorded. For this study, the Ru 3d, Si 2p, O 1s, and Ru 3d extended spectra are recorded at pass energies 100 eV and 300 eV. The spectra at pass energy of 300 eV and 100 eV are recorded with 4 frames each and a step size of 100meV and 50meV respectively. These spectra are called the high-resolution spectra and are used to characterize the chemical environment of different elements present at the surface of the samples. During the oxidation process, high-resolution spectra at a pass energy of 100 eV with 1 frame and a step size of 50 meV are used to carefully track the evolution of the species which is characterized as the in-situ spectra. The in-situ measurements and the described parameters allow for the acquisition of Ru 3d, Si 2p and O 1s spectra of high intensity with a short time resolution of 2.5 minutes between consecutive spectrum.

3.2.3. Data Analysis

3.2.3.1. XPS Data Fitting

The obtained spectra from XPS are analyzed using a peak fitting software called KolXPD. The first step for quantitatively analyzing XPS data is to do peak fitting for calculating the area of the peaks of the chosen atomic species. To obtain all fits, subtracting the background signal is important for accurately determining the correct area of all peaks recorded. To prevent over or under-estimation of peak area, Shirley background was used for subtracting the background signal. The second step is fitting the peak shape to the atomic transition to determine the area of the peak. The peak shapes of all atomic transitions recorded during XPS experiments are fitted with a convolution of the Cauchy-Lorentz distribution and the Gaussian distribution, also known as the Voigt Peak.

3.2.3.2. Interpretation and Qualitative Analysis

After subtracting the background and peak fitting, each peak area recorded during in-situ XPS measurements is normalized by dividing the peak area by the transition-specific photoionization cross-section of the element [3]. The value obtained is called the normalized peak area. XPS in-situ data records changes in chemical state and composition, approximately every 2.5 minutes, and is very useful in determining changes in chemical environment of the individual elemental species considered for this study. The normalized peak areas obtained from XPS spectra can only be used to obtain atomic ratios and cannot be used to determine the absolute density of sample' surface. The following formulas are used to calculate certain ratios and percentages that helped in determining the changes happening to individual atomic species during various experiments carried out for this project.

To determine the ruthenium silicide (Ru_xSi_y) compounds formed during the annealing of the samples, formula 1 was used:

$$\frac{Si}{Ru} = \frac{Normalized\ peak\ area\ of\ Si\ 2p\ spectra}{Normalized\ peak\ area\ of\ Ru\ 3d\ spectra} \quad (1)$$

In formula (1), the normalized peak (NP) area of Si 2p spectrum is divided by the NP area of Ru 3d spectrum. Doing this for the entire in-situ spectra recorded during the annealing of samples results in plotting of the Si/Ru ratio displayed in Figures 2A and 2B in the *Result* section.

To see the evolution of individual species during annealing and oxidation experiments, formula 2 was employed:

$$Atomic\ concentration\ of\ species\ A\ (\%) = \frac{NP\ area\ of\ species\ A\ \ spectum}{NP\ area\ of\ all\ species\ spectra} \quad (2)$$

Formula (2) states that the atomic concentration of an element A (Ru, Si or O) is given by dividing the NP area of species A spectrum by the NP area of all species including species A as well. Calculating the atomic concentration of each species using formula (2) ensures that evolution of atomic concentration observed in Figures 3A, 3B, 3C, 10A, 10B, and 10C in the *Results* section is further normalized to the entire NP area of all species involved during the annealing and oxidation experiments.

For calculating the oxygen content of each sample, formula 3 was used:

$$Oxygen\ Content\ (\%) = \frac{NP\ area\ of\ O\ 1s\ spectra}{NP\ area\ of\ all\ spectra\ including\ O\ 1s} \quad (3)$$

Formula (3) states that diving the normalized peak area under the O 1s spectrum and normalized peak area under Ru 3d + Si 2p + O 1s spectra gives the oxygen content at the surface of a sample. Thus, formula (3) is to plot the oxygen content plotted for all samples displayed in Figure 11A in the *Results* section.

3.2.3.3. Ruthenium fit

The fit of the Ru 3d XPS spectrum is shown in Figure 1A in the *Results* section. To obtain this fit, first, the Shirley background is implemented to subtract the background. The most significant peaks of Ru are the Ru $3d_{5/2}$ and Ru $3d_{3/2}$ peaks which are separated by 4.17 eV binding energy due to the spin-orbit coupling. This separation is fixed in the fitting parameters. Additionally, the area ratio between the $3d_{5/2}$ and $3d_{3/2}$ peaks is 3:2, which is also

fixed in our fitting parameters. Fixing these parameters is necessary since according to atomic physics the total angular momentum *J*, has values 5/2 and 3/2 for the Ru 3d orbital. The statistical weight of states $3d_{5/2}$ and $3d_{3/2}$ is calculated using the following formula (4):

$$2J+1 = \text{number of electrons in each orbital} \quad (4)$$

Dividing the number of electrons obtained using formula (4) for each state gives the area ratio of 3:2 between Ru $3d_{5/2}$ and Ru $3d_{3/2}$ orbitals. The Gaussian width for both the Ru peaks is kept equal in fitting parameters since the peak splitting does not cause any change in the Gaussian width of the peaks. However, the Lorentzian width of the two Voigt peaks is allowed to differ because the Ru $3d_{3/2}$ peak experiences the Coster-Kronig broadening effect [4], which effectively expands its Lorentzian width of the Ru $3d_{3/2}$ peak.

Metallic Ru peaks also have an asymmetric shape which is mainly because of the inelastic scattering of electrons and the creation of electron-hole pairs in the partially filled valence band of Ru. Due to this, the Voigt peak shape is not a perfect fit for metallic Ru. This can be directly observed from Figure 1A (*Results* section), where we see that the Voigt fit does not overlap perfectly with the obtained signal at the edges of the $3d_{5/2}$ and $3d_{3/2}$ peaks. The metallic Ru peaks could have been fitted using two Doniac-Sunjic-Gaussian convoluted asymmetric peaks, however this was not necessary since the detailed analysis of Ru metal is not the primary purpose of this project.

3.2.3.4. Ruthenium extended fit

The XPS spectrum of ruthenium is known to have characteristic plasmon (energy) loss features/peaks [5], which are also fitted using Voigt profiles in Figure 4A (*Results* section). Previous studies on XPS plasmon loss peaks of Ru have shown that plasmon loss features in the photoelectron spectra can be used for identifying compounds with different electronic structures [5]. Previous studies on ruthenium silicide compounds have shown that the formation of ruthenium silicide compounds upon annealing [5] results in changing the shape and position of the plasmon loss peaks detected in the Ru spectrum. The formation of ruthenium silicide compounds also results in the disappearance of asymmetry in Ru 3d XPS spectra. On the other hand, the formation of ruthenium oxide compounds formed from the oxidation of ruthenium results in the reappearance of asymmetry in the Ru 3d XPS spectrum [6].

3.2.3.5. Silicon fit

The fit for the Si 2p XPS spectrum of Si follows the same procedure as that of Ru. For the case of Si, the most dominant peaks are those of the 2p orbital, and thus the peaks observed in Figure 1D (*Results* section) are $2p_{3/2}$ and $2p_{1/2}$. The peak splitting due to spin-orbit coupling for these peaks is 0.6eV which is fixed in our fitting parameters. As discussed in the case of *Ruthenium* fit, the area ratio between the $2p_{3/2}$ and $2p_{1/2}$ peaks is calculated to be 2:1 using formula (4) and therefore also fixed in the fitting parameters.

In this research project, the oxidation of Ru_xSi_y compounds is analyzed. Therefore, the presence of Si_xO_y is expected and supported by previous literature [7, 8]. Although, the peak splitting corresponding to Si_xO_y has not been reported before because the silicon oxide peaks in the Si 2p XPS spectrum have a larger gaussian width than elemental silicon. This report shows that the Si_xO_y peak in the Si 2p spectrum also splits due to spin-orbit coupling.

The relative position between different species observed is always fixed because it helps differentiate the correct signal from the noise when analyzing the in-situ spectra. It also helps to identify when the evolution of individual atomic species started, thereby indicating the exact parameters and conditions that caused the transition to occur.

3.2.3.6. Oxygen Fit

The fit for the O 1s XPS spectrum follows the same procedure. In this case, the 1s orbital has the most dominant peak in the XPS spectra. The 1s orbital does not undergo spin-orbital splitting, and since the sample was annealed at 700°C for at least 80 minutes, no oxygen was present before starting the oxidation of the samples. After severe oxidation, the O 1s peaks corresponding to Si_xO_y compound formation and adsorbed oxygen were observed [9]. An additional peak corresponding to the formation of RuO_x compounds is reported and observed in Figure 7D (*Results* section). The significance of this peak will be further discussed in the *Discussion* section.

4. Results

4.1. Formation of ruthenium silicide compounds

To study the oxidation of ruthenium silicide compounds, it was essential to determine the stoichiometry of the compounds formed during the annealing of the samples. The initial spectra are called pristine because no oxygen and silicon species were detected at the surface of the samples after the deposition of metallic ruthenium on Si (100) substrate in ultra-high vacuum (UHV). Figure 1A shows the pristine high-resolution XPS spectrum of the Ru 3d region for sample A. From this graph, it was observed that pristine Ru 3d XPS spectrum has asymmetric Ru 3d peak shapes, and 2 Voigt peaks were used to fit the spectrum to identify the Ru species at the surface of the sample. It was also observable that Voigt peaks at BE of 279.7 (labelled Ru $3d_{5/2}$) and at BE of 283.9 (labelled Ru $3d_{3/2}$) do not fit the Ru 3d spectrum very well because of the asymmetry associated with PLD-deposited metallic ruthenium.

From the Si 2p XPS spectrum in Figure 1B, it was clearly observable that Si 2p spectrum in the pristine sample does not have any silicon species present at the surface of the sample. This was an expected result because 25 nm of ruthenium was deposited on top of the Si (100) substrate, and since the XPS is a surface-sensitive technique with a penetration depth of 5-10 nm, no other elements were expected and discovered at the surface of the pristine sample.

To study the oxidation behavior of ruthenium silicide compounds three samples were created using the deposition technique described in the Methods section. Since the deposition technique and parameters used for creating the three samples were equivalent, it was observed that the initial spectra of all three pristine samples were equivalent in all aspects. Therefore, figures 1A and 1B are representative of the Ru 3d and Si 2p XPS spectra for all three pristine samples.

For determining the oxidation characteristics of ruthenium silicide compounds, each sample was UHV annealed in the XPS measurement chamber to enable silicide formation at the surface of the sample [1]. Previous observations on the formation of ruthenium silicide compounds have shown that when a Ru layer on Si (100) is annealed for 1 hour at 625°C, only the Ru_2Si_3 phase is detected at the surface of the sample [1]. Therefore, all the samples analyzed were gradually heated up to 700°C using a radiative heater and kept at 700°C for at least 80 minutes to enable complete silicide formation.

To confirm that ruthenium silicide compounds formed at the surface of the first sample (called sample A), Figures 1C and 1D were plotted to show the high-resolution XPS spectra of Ru 3d and Si 2p regions respectively after UHV annealing Ru on Si (100) for a total of 225 minutes. The 225 minutes of UHV annealing of the sample included UHV annealing the sample at 700°C for 80 minutes. The Ru 3d spectrum after annealing of sample A was fitted using 3 Voigt peaks. The first observation from Figure 1C shows that after annealing of the pristine sample, the Ru 3d peak shapes become symmetric and fit almost perfectly using Voigt peaks. Second, a new unidentified peak (NUP) was observed to appear next to the Ru $3d_{3/2}$ peak, at +4.2eV away from the Ru $3d_{5/2}$ peak position. The NUP was also fitted using a Voigt peak. Observations from Figure 1D show that the dominant peak in the Si 2p spectrum was

observed to be the Si $2p_{3/2}$ peak at 99.5eV. Si $2p_{1/2}$ peak was also observed at +0.6 eV (100.1 eV) from the Si $2p_{3/2}$ peak. The second peak in the Si 2p spectrum is known to occur because of the spin-orbit splitting of the Si 2p orbital.

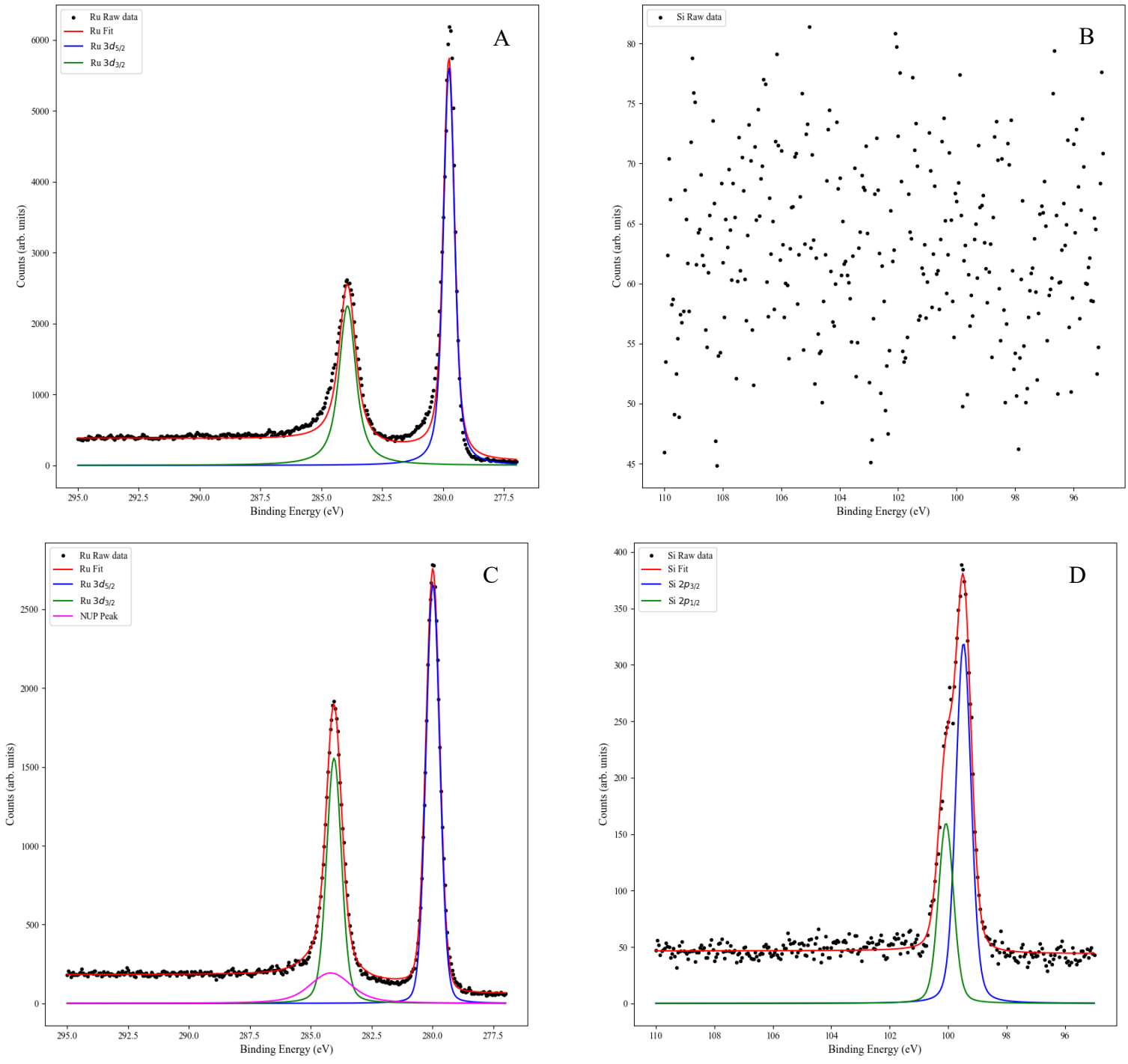

Figure 1: XPS spectra at pass energy 100 eV of (A) Ru 3d region for pristine sample A. (B) Si 2p region for pristine sample A. (C) Post-annealing Ru 3d region for sample A. (D) Post-annealing Si 2p region for sample A.

To determine how the atomic concentrations of Ru, and Si species evolved during UHV annealing of sample A , it was necessary to plot the evolution of Ru and Si species during the annealing process in Figure 2A. Figure 2A was plotted using the in-situ XPS annealing spectra and the atomic concentrations of each species was calculated using formula (2) described in the *Methods* section. From this figure, it was observable that the NUP first appeared at the 107.5 minute-mark, 37.5 minutes before the annealing temperature was fixed to 700°C at the 145-minute mark. From 145-minute mark onwards the sample was kept at the stable temperature of 700°C for the next 80 minutes. The atomic concentration of NUP at the sample's surface increased for 22.5 minutes (167.5-minute mark) in the stable temperature regime, after which the NUP growth saturated. From the same graph it was observable that the atomic concentration of total Ru and Si species at the sample's surface which was assumed to 100% and 0% respectively before the beginning of UHV annealing, first started decreasing (increasing for Si) at the 132.5 minute-mark, 12.5 minutes before the annealing temperature was fixed to 700°C. The atomic concentration of Ru decreased (increased for Si) for 30 minutes in the stable temperature regime (the 175-minute mark), and thereafter saturated.

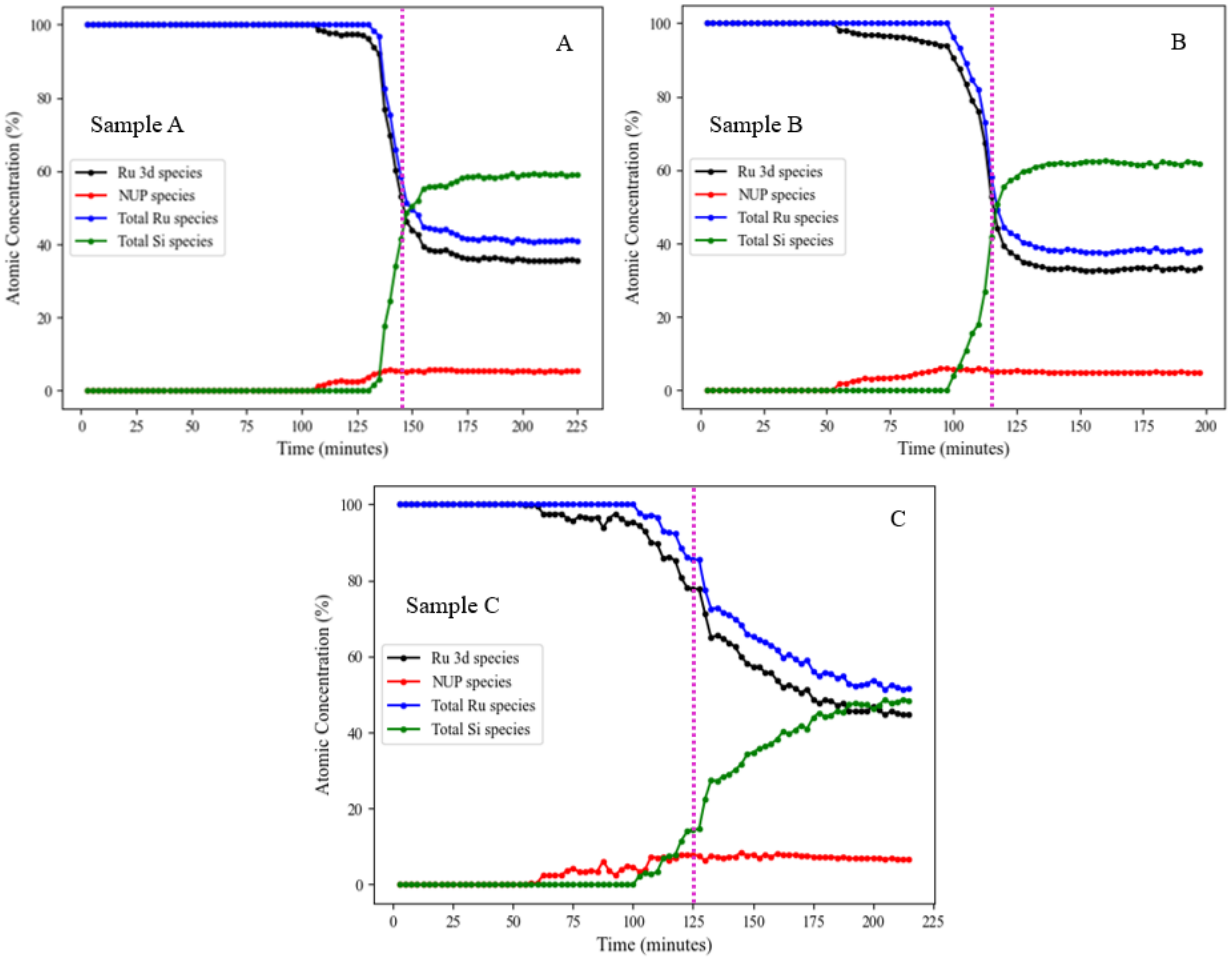

Figure 2: Evolution of Ru and Si species during annealing of (A) Sample A. (B) Sample B. (C) Sample C. The dashed line in each graph indicates the time when the annealing temperature was set to 700°C.

As mentioned above, three equivalent PLD-deposited Ru on Si (100) samples were created in UHV for this study. It was observed that for the other two samples B, and C, the post-annealing high-resolution Ru 3d and Si 2p XPS spectra look equivalent to the post-annealing high-resolution Ru 3d and Si 2p XPS spectra displayed in Figures 1C and 1D respectively for sample A. Therefore, the Ru 3d and Si 2p XPS spectra for samples B and C give us no new information about the formation of ruthenium silicide compounds. It is worth mentioning that the NUP position for both samples B, and C was now observed at +4.4 eV away from the Ru $3d_{5/2}$ peak position. Thus, the NUP position observed in samples B and C is +0.2eV ahead of the NUP position observed in sample A.

To confirm that the evolution of atomic concentration of individual species during UHV annealing of samples B and C followed the same trend as that of sample A, it was important to reproduce the results of Figure 2A for samples B, and C. Thus, Figures 2B and 2C were plotted to show the evolution of Ru, Si, and NUP species during annealing samples B and C respectively.

From Figure 2B it was observable that the evolution of all species during the annealing of sample B followed the same pattern as sample A in Figure 2A. In the case of sample B, the saturation point, for the decrease in the atomic concentration of Ru species and the increase in the atomic concentration of NUP and Si species at the surface, occurred 15 minutes after the annealing temperature was fixed at 700°C (at the 117.5-minute mark) at the 132.5-minute mark.

In the case of sample C, it was observed from Figure 2C that the evolution of all species during the annealing of sample C did not follow the same pattern as that of samples A and B. The decrease in atomic concentration of the Ru species and increase in the atomic concentration of Si species saturated 65 minutes after the sample annealing temperature was fixed at 700°C (at the 125-minute mark) which was at the 190-minute mark. While the increase in the atomic concentration of NUP, which started at appearing 55 minute-mark (70 minutes before the stable temperature regime) saturated 7.5 minutes after the sample's annealing temperature was fixed at 700°C at the 132.5-minute mark. Although the total annealing time observed in Figures 2A, 2B, and 2C is different, this should not affect the synthesis of the ruthenium silicide compound formation because all three samples were UHV annealed for 80 minutes at 700°C, thereby overcoming the experimental methods limitations. This is also one of the reasons that there is a difference in the time at which the saturation point for each species occurs between samples A, B, and C.

The evolution of the Si/Ru ratios vs time was plotted in Figure 3A and shown in Table 1, was obtained by analyzing the in-situ data gathered during the annealing of samples and formula (1) described in the *Discussion* section. From this graph, it was observed that the Si/Ru ratio for sample A was 1.4, for sample B was 1.6, and 0.90 for sample C. It was also observed that the evolution of the Si/Ru ratio for samples A and B was fast compared to the evolution of Si/Ru observed for the case of sample C, which was slow. Additionally, the Si/Ru ratio for sample C did not reach a saturation point, even though the sample was UHV annealed for 90 minutes to enable silicide formation. Finally, it was expected and observed that the time at which the Si/Ru ratios reached an equilibrium value in Figure 3A, coincided with the time at which the atomic concentration Si species at the surface of the sample reached the saturation point in Figures 2A, 2B, and 2C.

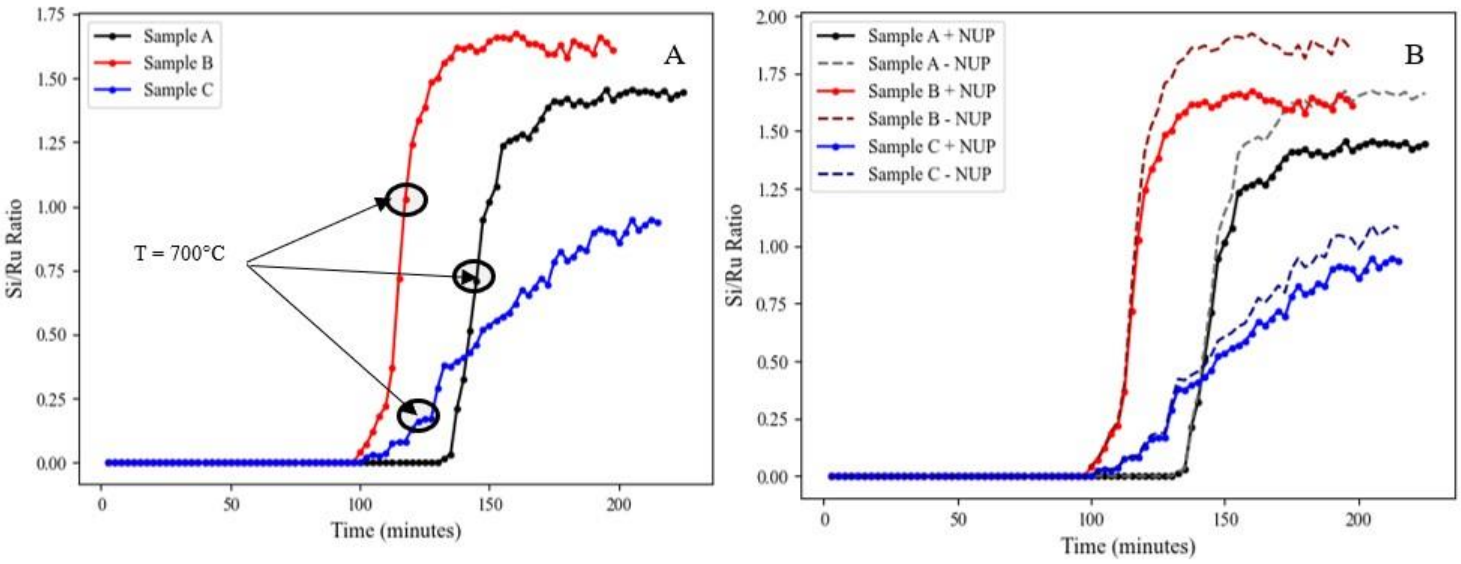

Figure 3: Evolution of Si/Ru ratio for all samples (A) Including NUP. (B) Including and excluding NUP magnitude. The time when the sample's temperature is set to 700°C is circled in Figure 3A.

Sample Name	Si/Ru (pristine)	Si/Ru (annealed) including NUP	Si/Ru (annealed) excluding NUP
A	0	1.5	1.9
B	0	1.4	1.7
C	0	0.9	1.1

Table 1: Si/Ru ratios for all samples observed after samples were annealed at 700 C for at least 80 minutes.

To identify the impact of the NUP on the Si/Ru ratio observed in Figure 3A, the Si/Ru ratio for all samples was again plotted in Figure 3B. Figure 3B shows the Si/Ru ratio for all samples when the NUP magnitude was included in calculating the Si/Ru ratio (dash-dot lines) and when the NUP magnitude was excluded from the ratio calculations (dashed lines). From Figure 3B and Table 1, it was observable that for all samples, the Si/Ru ratio value including NUP magnitude is lower than the Si/Ru ratio value excluding NUP magnitude.

To confirm the stoichiometric ratio of ruthenium silicide compounds fabricated after completion of the annealing process the high-resolution Ru 3d extended XPS spectrum were recorded for each sample. Previous observations have shown that the conversion of metallic ruthenium to ruthenium silicide species is accompanied by changes in the shape and position of the plasmon loss peaks known to exist in the extended XPS photoelectron spectrum of ruthenium [2]. The change in the position of the plasmon loss peak is tracked by calculating the change in distance between the position of Ru $3d_{5/2}$ peak position and the plasmon loss peak position, before and after annealing for all samples (Table 2).

Sample Name	PL peak positions for pristine sample (eV)	PL peak positions post-annealing (eV)	PL peak positions post-oxidation (eV)
A	+8.0, +29.4	+22.5, +26.7	+22.5, +26.7
B	+8.0, +29.4	NA	+21.6, +25.8
C	+8.0, +29.4	+23.5, +27.7	+23.5, +27.7

Table 2: Plasmon-loss (PL) peak positions observed for all samples relative to the Ru 3d5/2 peak position.

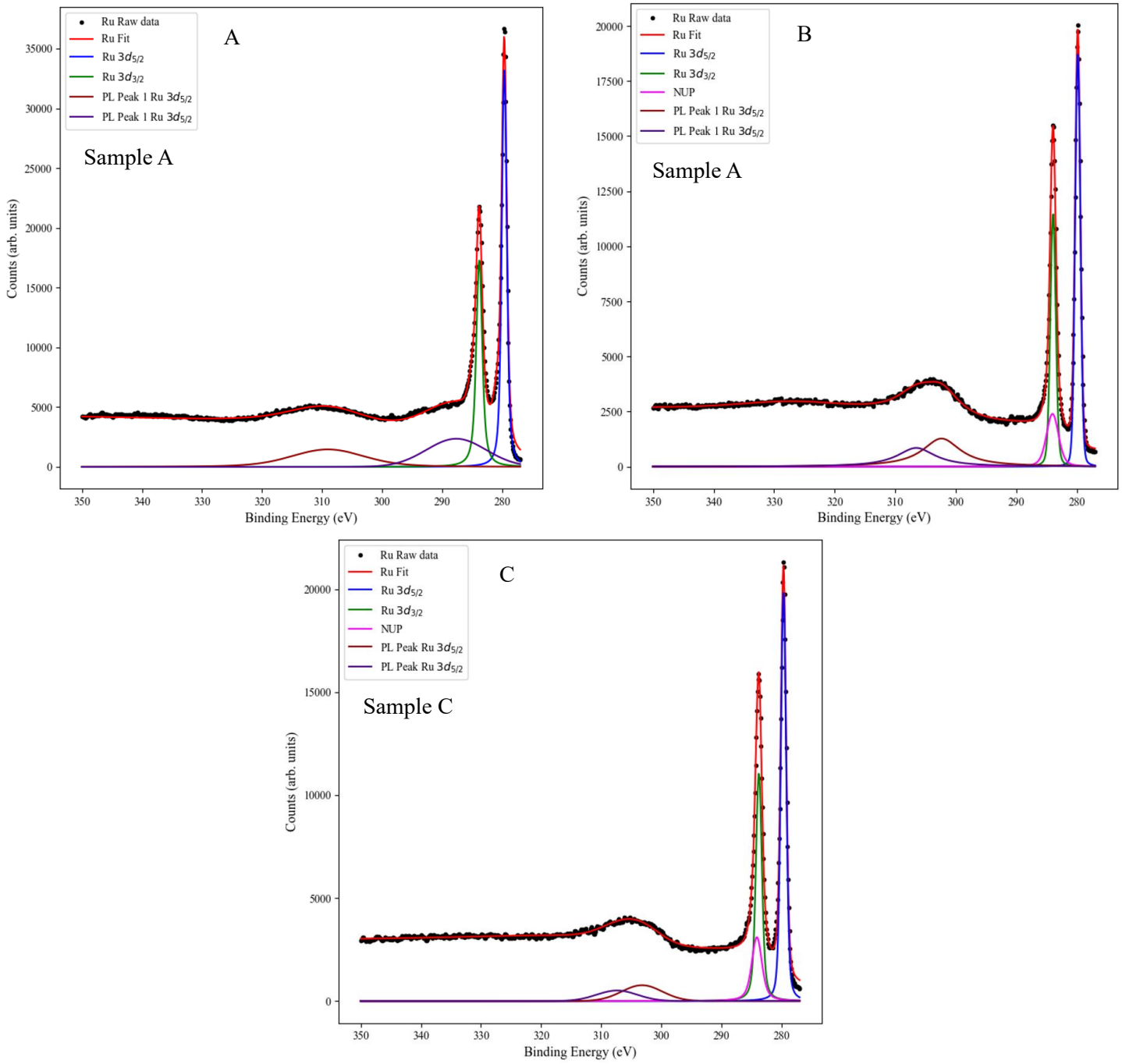

Figure 4: High-resolution Ru 3d extended XPS spectra at pass energy 300 eV of (A) Pristine sample A. (B) Sample A post-annealing. (C) Sample C post-annealing.

The Ru 3d extended high-resolution XPS spectrum observed in Figure 4A shows that the pristine samples have two plasmon loss peaks at positions +8.0 eV and +29.4 eV away from the Ru $3d_{5/2}$ peak position. From Figure 3A it was observed that the Si/Ru ratio obtained for each sample is different, thereby giving a reason to suspect that the ruthenium silicide compounds formed at the surface of every sample have a different stoichiometric ratio. Thus, the post-annealing high-resolution Ru 3d extended spectra for samples A, and C were plotted in Figures 4B and 4C respectively. From Figure 4B, it was observed that after annealing of sample A, the plasmon loss peak positions shifted to +22.5 eV and +26.7eV away from the Ru $3d_{5/2}$ peak position. And, for sample C, the plasmon loss peak positions after annealing of the sample, were observed at +23.5 eV and +27.7eV away from the Ru $3d_{5/2}$ peak position. In the case of sample B, the reference Ru 3d extended XPS spectrum post-annealing of the sample were not recorded due to a recording error during experimentation and was characterized as a random error. Therefore, the stoichiometric Si/Ru ratio observed for sample B from the extended Ru 3d XPS spectrum will be discussed in the next section.

4.2. Oxidation of Ruthenium Silicide

Before the start of the oxidation experiments, no oxygen species were detected at the surface of any sample because all samples were UHV annealed at 700°C for at least 80 minutes as mentioned in the above section. Therefore, the O 1s reference XPS spectrum displayed in Figure 7A shows the absence of any oxygen species before oxidation of all the samples.

To determine how the thermal oxidation on ruthenium silicide compounds and causes oxidation of Ru and Si species, all samples produced during the annealing process were exposed to stepwise increments of oxygen gas pressures at a fixed temperature. Before starting thermal oxidation experiments, each sample's surface temperature was set to a fixed value using the radiative heater, and the temperature of the sample was confirmed using an infrared pyrometer. The pressures and the temperatures that each sample was exposed to are displayed in Table 3. Table 3 also shows the amount of time a sample was kept at a certain pressure. Figure 5B shows the after-oxidation high-resolution Ru 3d XPS spectrum of sample A, after it was thermally oxidized at 350°C for 317.5 minutes. For this sample, no new ruthenium peaks/species were observed, and the shape of the previously observed peaks in the Ru 3d spectrum remained unchanged. The NUP position also remained unchanged and was again observable at +4.2 eV away from the Ru $3d_{5/2}$ peak position.

Sample Name	Thermal Oxidation Temperature (°C)	Exposure time at different O_2 pressures (minutes)		
		$P = 1.2 \times 10^{-4}$ mbar	$P = 1.2 \times 10^{-3}$ mbar	$P = 5.3 \times 10^{-3}$ mbar
A	350	100	100	105
B	700	107.5	100	100
C	550	110	120	105

Table 3: Stepwise thermal oxidation of the ruthenium silicide samples at different O_2 pressures.

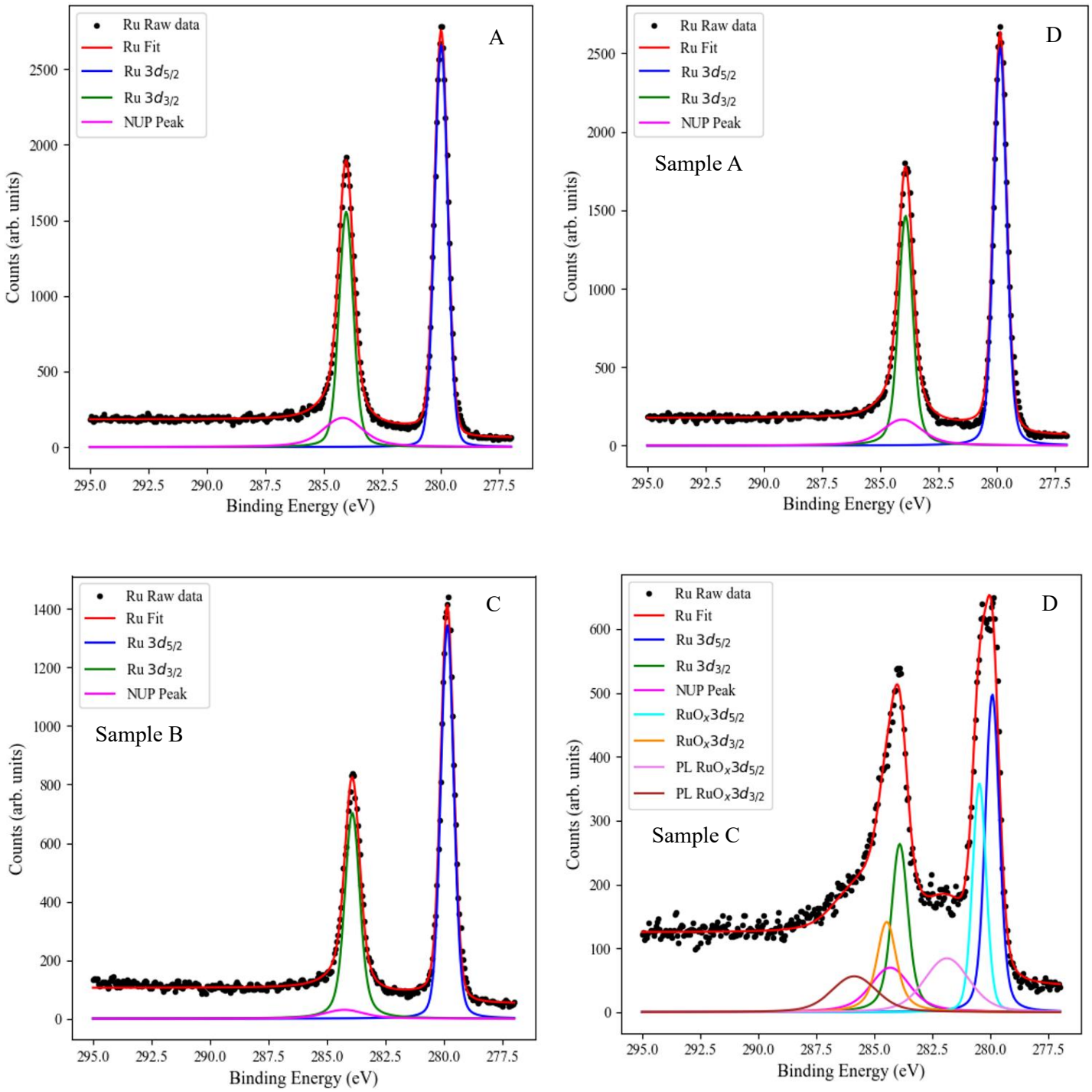

Figure 5: High-resolution XPS spectra of Ru 3d region at pass energy 100 eV of (A) All samples before thermal oxidation. (B) Sample A after oxidation. (C) Sample B after oxidation. (D) Sample C after oxidation.

Continuing with the results of sample A, Figure 6B shows the post-oxidation high-resolution Si 2p XPS spectrum of the sample. From this figure, it was observed that oxidation of the sample, results in the emergence of a new peak which gets split into two parts because of spin-orbit coupling split of Si 2p peaks. The peaks are observed at 102.2 eV (labelled – Si_xO_y – 3/2) and 102.8 eV (labelled Si_xO_y–1/2) in the Si 2p XPS spectrum, thereby indicating the formation of a new silicon species at the sample's surface. To confirm that the appearance of a new peak in the Si 2p spectrum and the absence of any new peaks in the Ru 3d spectrum

indicate the formation of new Si_xO_y species, the post-oxidation high-resolution O 1s XPS spectrum for sample A was plotted in Figure 7B. From this figure it was observed that two new peaks at 531.7eV (labelled – O– Si_xO_y) and 529.9 eV (labelled – O– adsorbed) appear in the O 1s spectrum of sample A, thus indicating the formation of new oxygen species at the sample's surface.

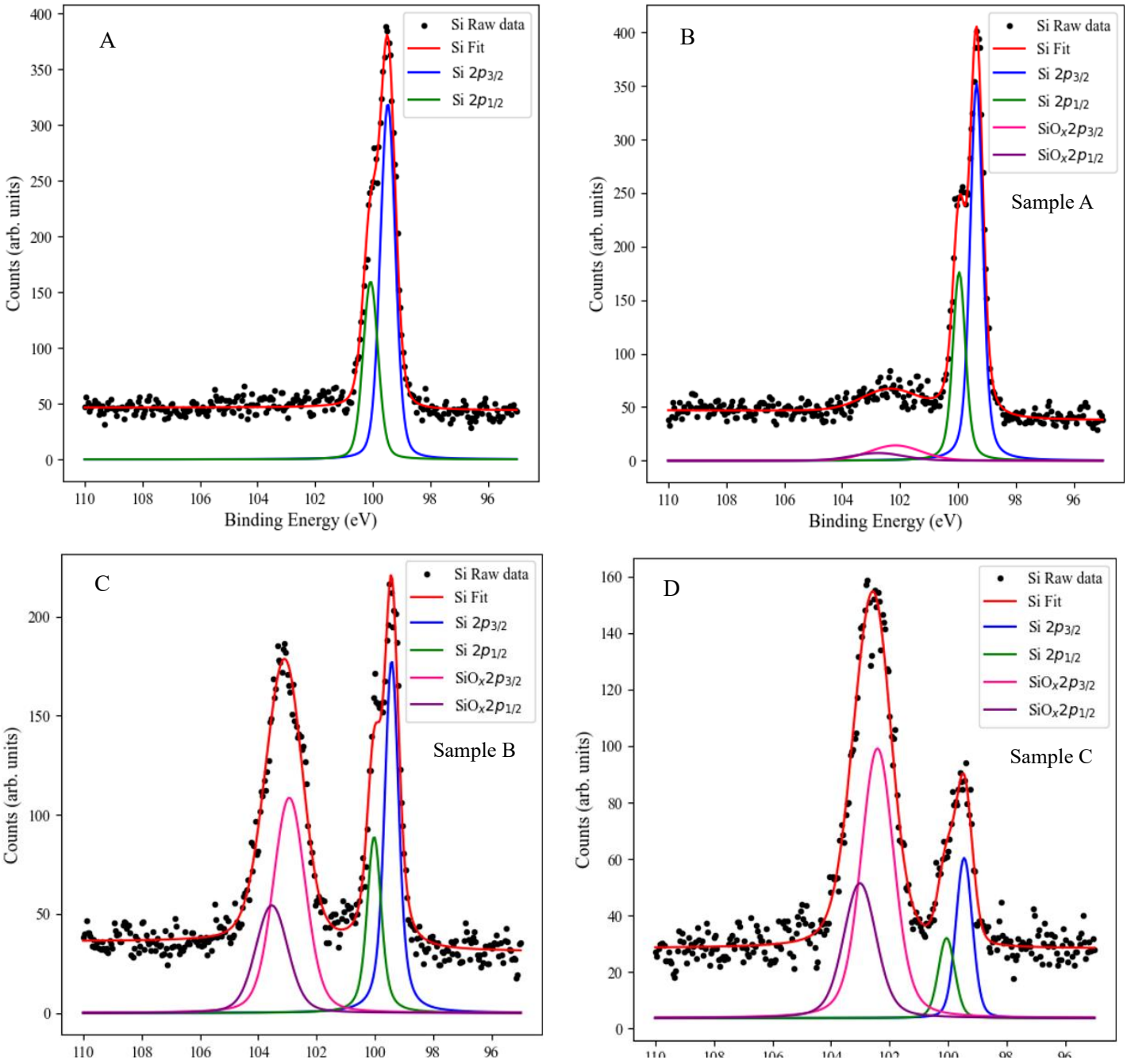

Figure 6: High-resolution XPS spectra of Si 2p region at pass energy 100 eV of (A) All samples before thermal oxidation. (B) Sample A after oxidation. (C) Sample B after oxidation. (D) Sample C after oxidation.

To confirm that the ruthenium silicide compounds, formed during UHV annealing of sample A, did not oxidize and change their stoichiometric ratios during the oxidation process, the after-annealing and after-oxidation high-resolution extended Ru 3d XPS spectrum were plotted in figure 8A and 8B respectively. From Figure 8B it was observable that the plasmon loss peak positions observed in the post-oxidation Ru 3d XPS spectrum of sample A remained unchanged. It was also observed that the ratio between NP area of PL peaks and to the rest of Ru species did not change.

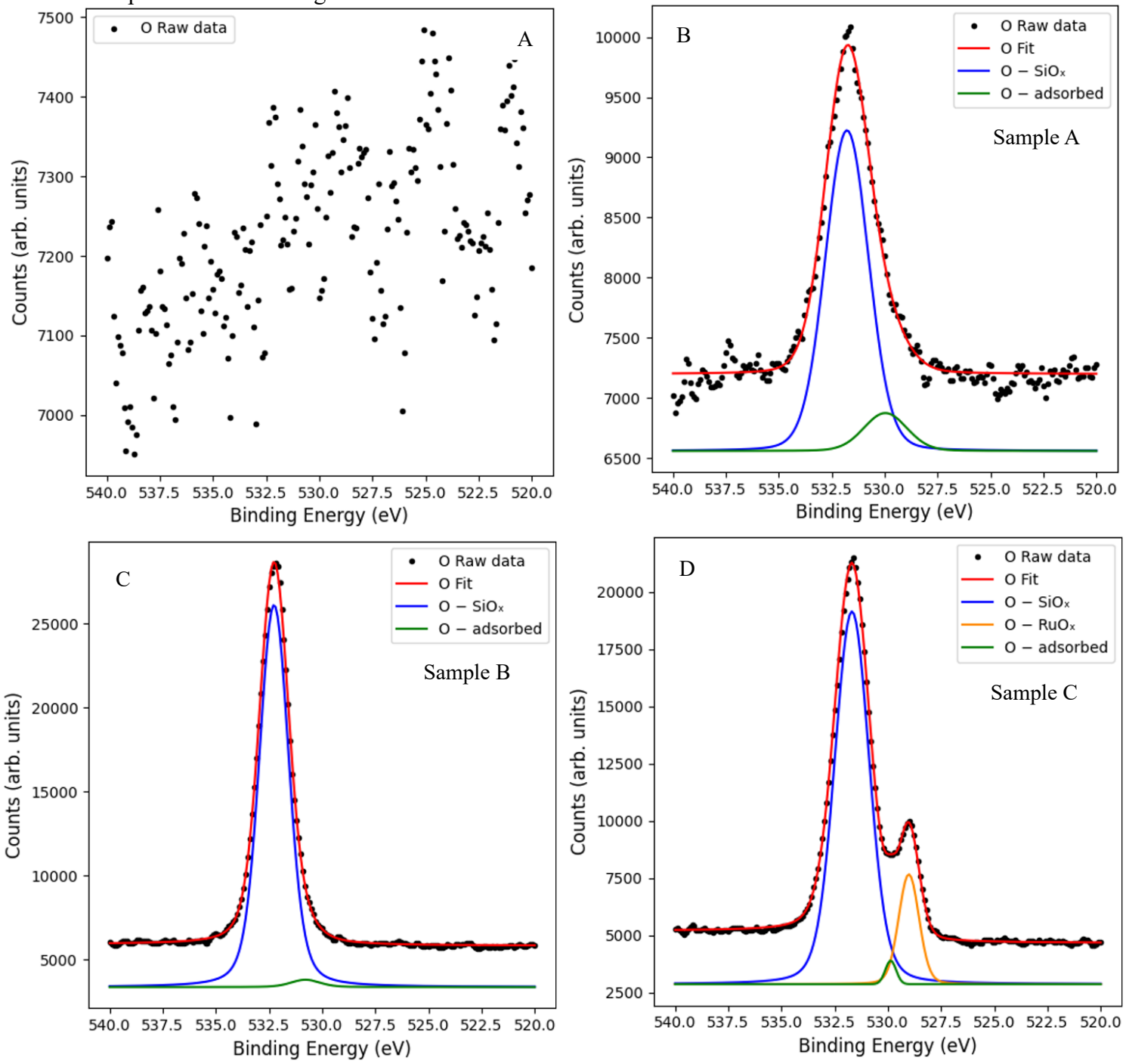

Figure 7: High-resolution XPS spectra of O 1s region at pass energy 300 eV of (A) All samples before thermal oxidation. (B) Sample A after oxidation. (C) Sample B after oxidation. (D) Sample C after oxidation.

After observing no clear indication that the ruthenium in Ru_xSi_y oxidized at 350°C and varying pressures, thermal oxidation of sample B was performed at 700°C for 310 minutes and varying oxygen pressures to determine whether the oxidation of ruthenium silicide compounds (in addition to oxidation of Si to form Si_xO_y) causes Ru in Ru_xSi_y to oxidize at a much higher temperature. Thus, all figures produced for sample A were also generated for sample B.

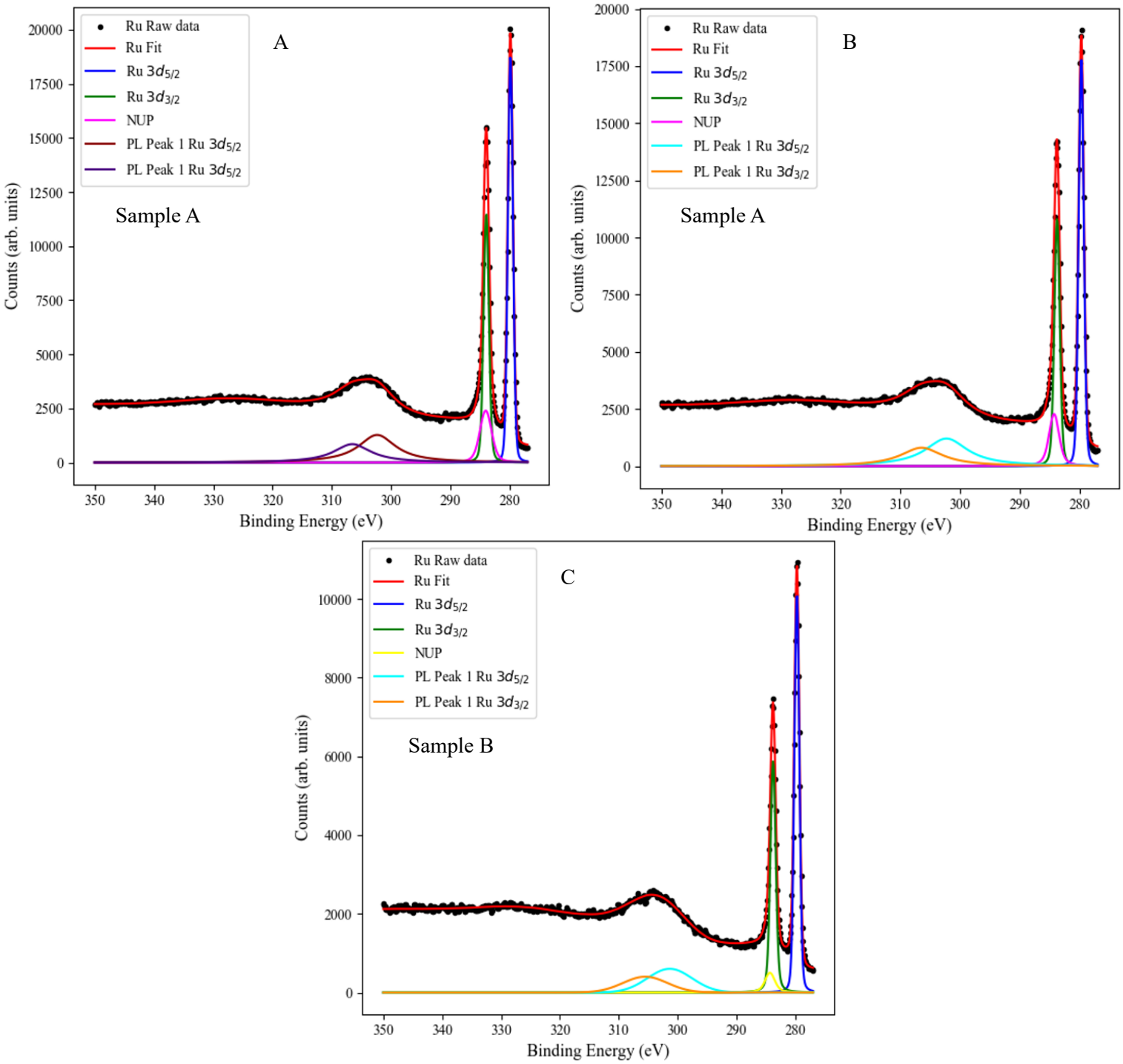

Figure 8: High-resolution Ru 3d extended XPS spectra at pass energy 300 eV of (A) Sample A post-annealing. (B) Sample A post-oxidation. (C) Sample B post-oxidation.

Table 3 shows that the only difference between the thermal oxidation of sample A and that of sample B was the temperature at which the two samples were oxidized. To determine how ruthenium silicide compounds oxidize at a higher temperature, the after-oxidation high-resolution Ru 3d XPS spectrum of sample B was plotted in Figure 5C. From Figure 5C it was observable that the Ru 3d XPS spectrum for sample B, like that of sample A, did not show the emergence of any new Ru peaks/species after oxidation of the sample. The NUP peak position also remained unchanged.

On the other hand, from Figure 6C it was observable that the Si 2p spectrum of sample B, like sample A, has one new peak divided into parts because of spin-orbit coupling split of Si 2p peaks in XPS. The peaks are observed at 102.9 eV (labelled Si_xO_y – 3/2) and 103.5 eV (labelled Si_xO_y – ½) indicating the formation of a new silicon species at the surface of the sample after oxidation. Again, due to the absence of any new Ru species in the Ru 3d XPS spectrum and the presence of new Si species in the Si 2p XPS spectrum, it was important to plot the after-oxidation high-resolution O 1s XPS spectrum in Figure 7C to determine the Si_xO_y species formed at the surface of sample B after it was thermally oxidized. From Figure 7C, it was revealed that the O 1s XPS spectrum of sample B, like sample A, has two new peaks at 532.4eV (labelled – O– Si_xO_y) and 531.2eV (labelled – O– adsorbed) indicating the formation of new oxygen species at the sample's surface.

To confirm that the ruthenium silicide compounds formed during the annealing of sample B did not undergo oxidation and their stoichiometric ratios remained unchanged during the oxidation experiment, the after-oxidation high-resolution extended Ru 3d XPS spectrum was plotted in Figure 8C. It was observed that the plasmon loss peaks after oxidation of the sample appear at +21.6 eV and +25.8 eV away from the Ru $3d_{5/2}$ peak position. From table 2, it was observable that the PL peak position observed for sample B post-oxidation is close to PL peak position observed for sample A post-annealing and post-oxidation. This observation gives the indication that the ruthenium silicide compounds formed at sample B's surface must be similar to those formed on the surface of sample A.

The last experiment was conducted to determine whether ruthenium silicide compounds oxidized at an intermediate temperature between 350°C and 700°C. It is important to mention that even though all data for sample C was recorded accurately, the determination of which Ru_xSi_y compounds formed at sample C's surface was only determined after the completion of oxidation experiments.

Sample C was oxidized at 550°C for 337.5 minutes and the stepwise increment in oxygen pressure was made in similar time intervals, as was done for samples A and B. From the after-oxidation high-resolution Ru 3d XPS spectrum, displayed in Figure 6D, it is clear that the oxidation of sample C resulted in the peak shapes of Ru 3d spectrum becoming asymmetric. From Figure 5D, it is also observable that the oxidation of this ruthenium silicide sample led to the emergence of four additional peaks in the Ru 3d XPS spectrum, indicating the formation of new Ru species at the sample's surface. The four new peaks appearing at 280.5 eV (labelled – Ru_xO_y 5/2), 284.5 eV (labelled – Ru_xO_y 3/2), 281.9 eV (labelled – PL Ru_xO_y 5/2), and 285.9 eV (labelled – PL Ru_xO_y 3/2) are labelled and visible in figure 6D and their location are typically attributed to the formation of Ru_xO_y compounds.

Figure 6D shows that, like in the case of samples A, and B, a new peak, split into two parts also appear in the Si 2p XPS spectrum at 102.4 eV (labelled Si_xO_y – 3/2) and 103.0 eV (labelled Si_xO_y – 3/2), indicating the formation of new silicon species at the sample C's surface. Following the same procedure for sample C, as for samples A and B, the reference spectrum for O 1s was plotted in Figure 7C. The O 1s spectrum was observed to have 3 new peaks at 531.8 eV (labelled – O– Si_xO_y), 529.5 eV (labelled – O– Ru_xO_y), and 528.9 eV (labelled – O–adsorbed) indicating the formation of new oxygen species at the sample's surface.

To illustrate the changes that occurred in stoichiometric ratio of ruthenium silicide compounds during thermal oxidation of sample C, the post-annealing and post-oxidation high-resolution extended Ru 3d XPS spectra of sample C were plotted in Figures 9A and 9B respectively. From this graph it was observed that the plasmon loss peak positions after oxidation of the sample remained unchanged, while the shape of the PL peaks changed slightly possibly indicating that the stoichiometric ratio of the ruthenium compounds remained changed during thermal oxidation of sample C.

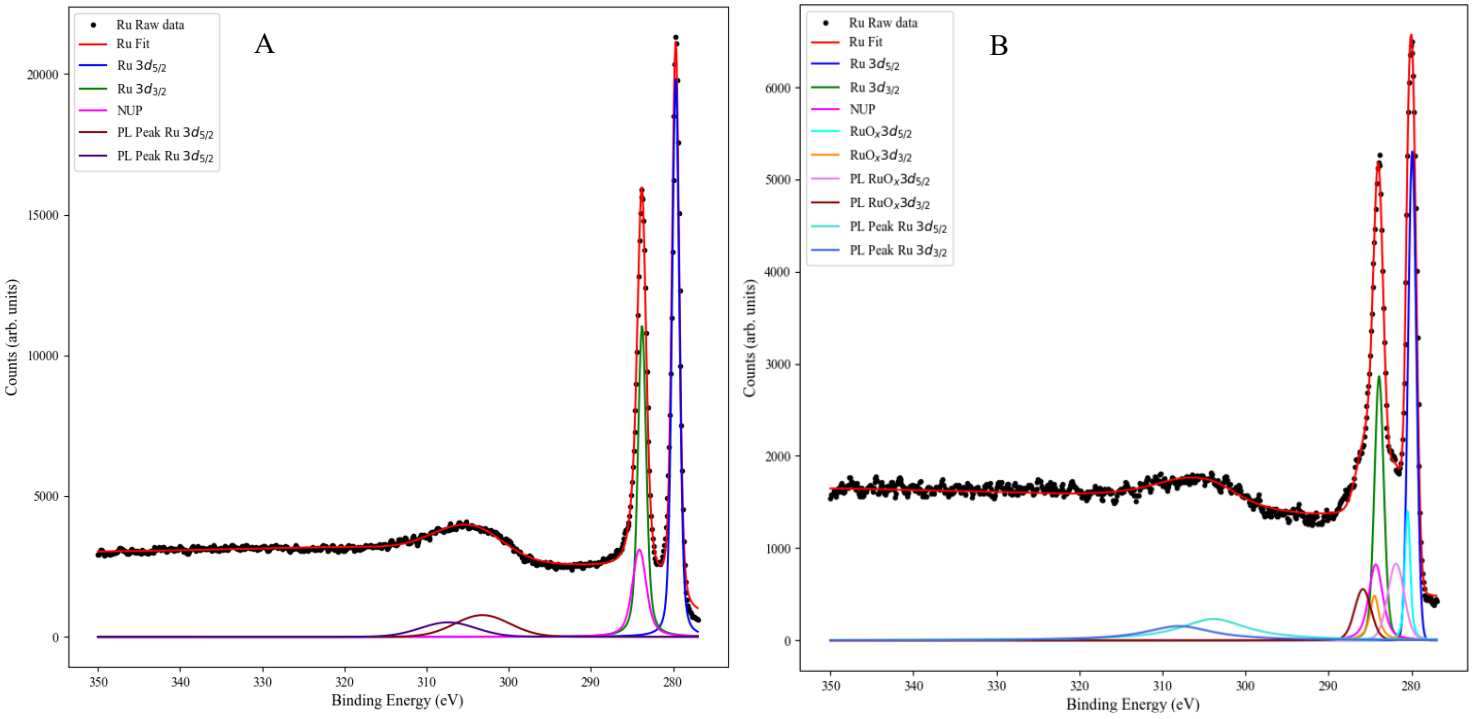

Figure 9: High-resolution Ru 3d extended XPS spectra at pass energy 300 eV of (A) Sample C post-annealing. (B) Sample C post-oxidation

To quantitatively compare the evolution of Ru, Si, and O species during thermal oxidation of samples A, B, and C, the atomic concentration of each species was plotted in Figures 10A, 10B and 10C respectively.

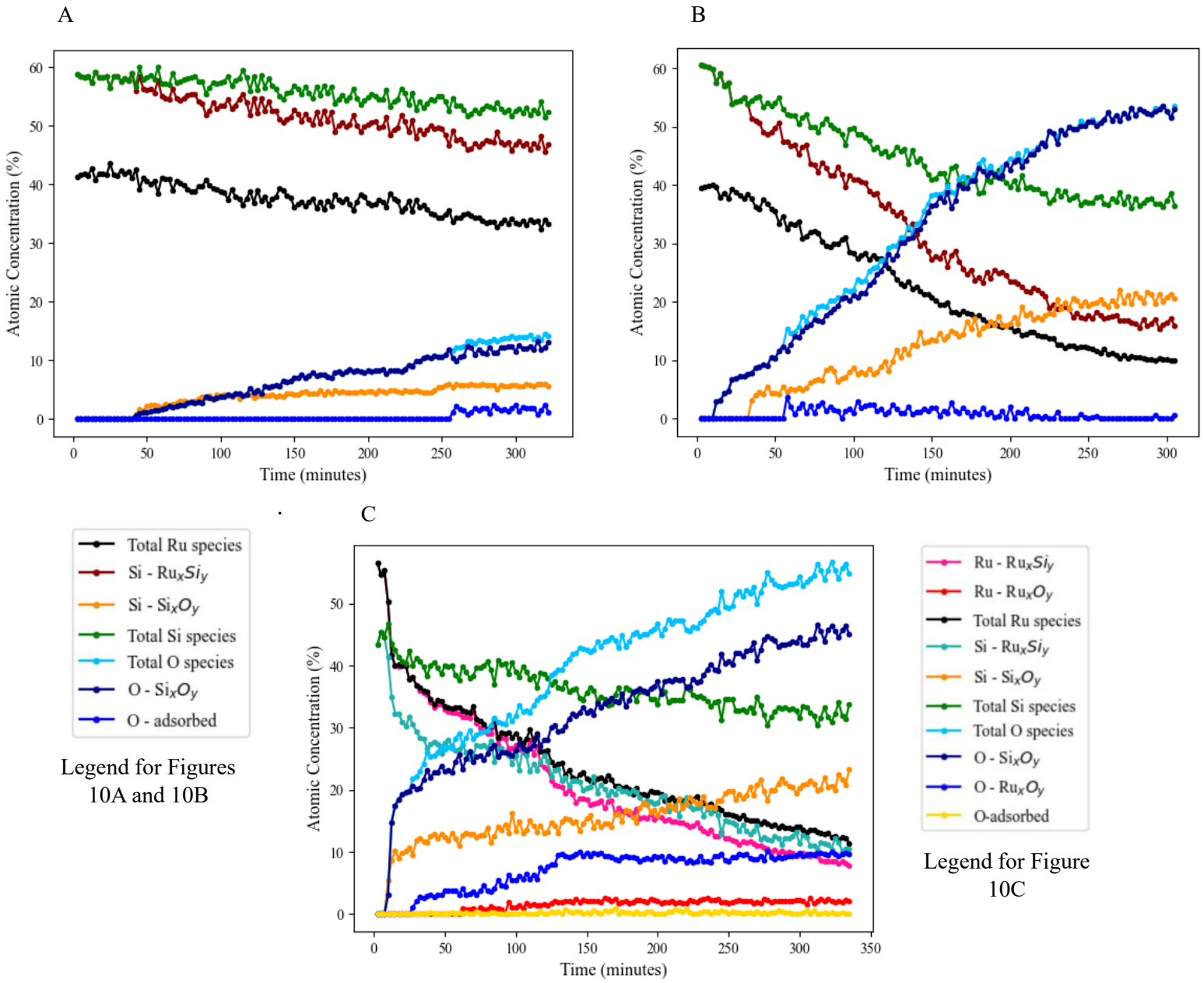

Figure 10: Evolution of Ru, Si, and O species during oxidation of (A) Sample A. (B) Sample B. (C) Sample C. The sectors created using dashed lines in the above Figures indicate the O_2 pressure during thermal oxidation of the samples. From the black dotted line until the pink dotted line P_{O_2}= 1.2 x 10^{-4} mbar. From the pink dotted line until the red dotted line P_{O_2}= 1.2 x 10^{-4} mbar, and from red dotted line until the end P_{O_2}= 5.3 x 10^{-3} mbar. The legend below Figure 10A, corresponds to Figures 10A and 10B. The legend below Figure 10B, corresponds to Figure 10C.

From Figure 10A, it was observable that the total amount of Ru species, the total amount of Si species, and the Si species labelled Si–Ru$_x$Si$_y$, decreased until 245-minute mark, and thereafter atomic concentration of these species saturated. The saturation point for total Ru, total Si and Si–Ru$_x$Si$_y$, occurred 23 minutes after the oxygen pressure was increased to 5.3 x 10^{-3} mbar. On the other hand, it was observed that the increase in the atomic concentration of the new Si species, labelled Si– Si$_x$O$_y$ in Figures 6B and 10A, saturated at two points. The first saturation point was reached 42.5 minutes after the oxygen pressure was increased to 1.2 x 10^{-3} mbar at the 157.5–minute mark, and the second saturation point was observed 37.5 minutes after the oxygen pressure was increased to 5.3 x 10^{-3} mbar at the 255–minute mark.

From figure 10 A, it was also observable that the atomic concentrations of total O species and the oxygen species labelled of O– Si_xO_y species (Figure 7B) increased up to 177.5-minute mark when the oxygen pressure was 1.2 x 10^{-3} mbar. After this point, the atomic concentration of these species saturated for 45 minutes. The atomic concentration of the species started increasing again from the 225-minute mark, 7.5 minutes after the oxygen pressure was increased to 5.3 x 10^{-3} mbar. After 225-minute mark, the atomic concentration of these two species did not a saturation point. Finally, it was also observable that the second peak (labelled O–adsorbed) that appeared in the O 1s spectrum displayed in Figure 7B, only starts appearing at the 257.5–minute mark and the growth of this species saturates very quickly at the 260–minute mark when oxygen pressure was already 5.3 x 10^{-3} mbar.

From Figure 10B, it was observed that the decrease in the atomic concentration of total Ru, total Si, and the Si species labelled Si–Ru_xSi_y species had a much larger slope than that of sample A but unlike sample A, the decrease in the atomic concentration these species did not saturate at any oxygen pressure mentioned in table 3. On the other hand, Figure 10B shows that the atomic concentration of total O, O– Si_xO_y, Si– Si_xO_y species keeps increasing without saturating at any oxygen pressure mentioned in table 3. It was also observable that the second oxygen species labelled O-adsorbed in Figure 7C, appeared at the 57.5–minute mark, and like sample A, the atomic concentration of O-adsorbed species saturated almost immediately at the 60–minute mark.

From Figure 10C, it was observed that the decrease in the atomic concentration of total Ru, Ru–Ru_xSi_y, and, Si–Ru_xSi_y species almost have the same slope, and like in the case of sample B, the decrease in the atomic concentration of these species did not saturate at any pressure during thermal oxidation of sample C at 550°C. Further, it was observed that the growth of combined atomic concentration of the new Ru species (Ru_xO_y 5/2, Ru_xO_y 3/2, PL–Ru_xO_y 5/2, and PL–Ru_xO_y 3/2 in figure 6D) labelled Ru–Ru_xO_y, and the growth of the atomic concentration of the new O species labelled O–Ru_xO_y saturates at the 145-minute mark, 27.5 minutes after the oxygen pressure was increased to 1.2 x 10^{-3} mbar. After the 145-minute mark, no increase in the atomic concentration of either species was observable, even though the pressure was increased again to 5.3 x 10^{-3} mbar at the 227.5-minute mark. Figure 10C, also shows that the decrease in the atomic concentration of total Si species first saturates around the 147.5–minute mark, 30 minutes after the oxygen pressure was increased to 1.2 x 10^{-3} mbar. The atomic concentration of total Si species starts decreasing again at the 227.5-minute mark, the time when the oxygen pressure was increased to 5.3 x 10^{-3} mbar, and thereafter saturated at the 272.5-minute mark until the end of thermal oxidation. On the other hand, it was also observable that the growth in the atomic concentration of Si–Si_xO_y, O–Si_xO_y, and total O species does not reach a saturation point at any oxygen pressure.

To determine the oxygen content (described in formula (3) in the *Methods* section), of each sample, figure 11A was plotted show how the oxygen content varies during thermal oxidation of each sample. The oxygen content for sample C, oxidized at 550°C, oxidized with a maximum value of 56.6%. However, the increase in oxygen content for sample C did not saturate at any time and pressure during the thermal oxidation process. Sample B, which was oxidized at the maximum temperature of 700°C, was observed to have a maximum oxygen content of 52.1%, and like sample C the oxygen content did not saturate at any time. Finally, the lowest percentage of oxidation was observed for sample A, which was oxidized at 350°C, and 14.6% oxygen content was observed. However, it was observed that the oxygen content

for sample A saturated at the 177.5-minute mark, when the oxygen pressure was 1.2 x 10^{-3} mbar. The oxygen content started increasing 10 minutes after the oxygen pressure was increased to 5.3 x 10^{-3} mbar and thereafter never saturated again.

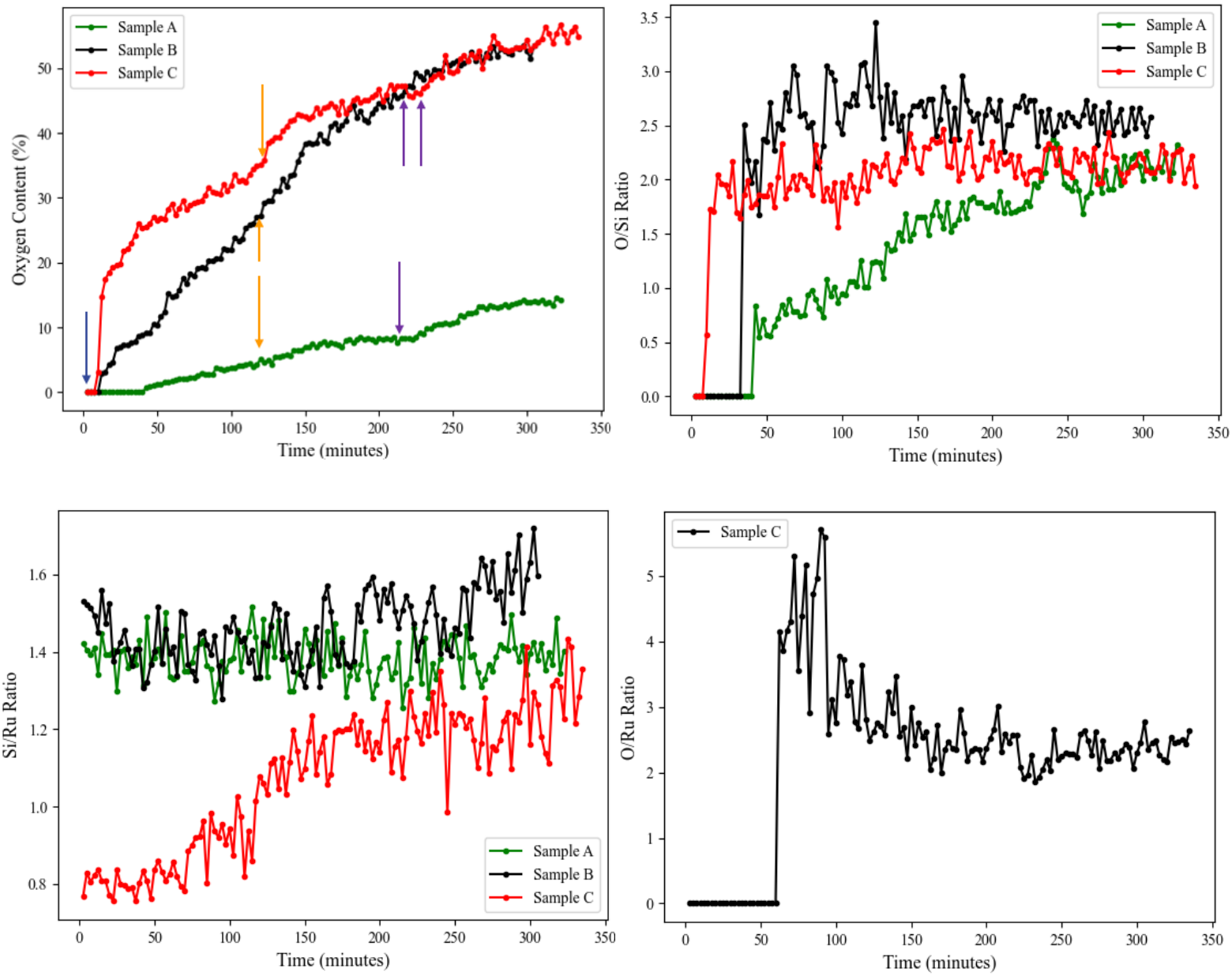

Figure 11: Evolution of (A) Oxidation percentage during oxidation of all samples. (B) O/Si ratio during oxidation of all samples. (C). Si/Ru during oxidation of all samples. (D) O/Ru ratio during oxidation of sample C. In the above Figures, the different coloured arrows indicate the O_2 pressure during the thermal oxidation of the samples. The blue arrows at the beginning of each graph indicate the time when oxygen pressure was set to P_{O_2}= 1.2 x 10^{-4} mbar. The orange arrows indicate the time where oxygen pressure was increased to P_{O_2}= 1.2 x 10^{-4} mbar, and the purple arrows indicates the point where oxygen pressure was increased to P_{O_2}= 5.3 x 10^{-3} mbar.

To determine the Si_xO_y species formed during the oxidation of each sample, figure 11B was plotted to show the evolution of the normalized intensity ratio between peaks Si– Si_xO_y 3/2 and Si– Si_xO_y ½ observed in the Si 2p XPS spectra in Figures 6B, 6C, and 6D and peak O–Si_xO_y observed in the O 1s XPS spectra in figures 7B 7C, and 7D during oxidation of samples A, B and C. Figure 11B, showed that the O/Si ratio for sample A reaches an equilibrium value of 2.1 around the 235–minute mark, which was 17.5 minutes after the oxygen pressure was increased to 5.3 x 10^{-3} mbar. On the other hand, the O/Si ratio for samples B, and C reached an equilibrium value of 2.5 and 2.1 respectively around the 150–minute mark when the oxygen pressure was still 1.2 x 10^{-3} mbar.

To observe the change in the Si/Ru ratio after oxidation of each sample, figure 11C was plotted and it shows the evolution of normalized intensity ratio between peaks Ru–Ru_xSi_y 5/2, Ru–Ru_xSi_y 3/2, and NUP observed in the Ru 3d XPS spectra (Figures 5B–5D) and peaks Si–Ru_xSi_y 3/2 and Si–Ru_xSi_y 1/2, observed in the Si 2p XPS spectra (Figures 6B–6D) during oxidation of each sample. From Figure 11C, it was observed that the Si/Ru ratio for samples A, and B did not change during oxidation of these two samples. On the other hand, it was observed that the Si/Ru ratio for sample C increased from the initial value of 0.9 to 1.2. It was also observed that the saturation point for the increase in the Si/Ru ratio for sample C, coincides with the saturation points of the decrease in the atomic concentration of total Si species observed in Figure 10C.

Finally, due to the emergence of new Ru species (Ru_xO_y 5/2, Ru_xO_y 3/2, PL–Ru_xO_y 5/2, and PL–Ru_xO_y 3/2) in the Ru 3d XPS spectrum of sample C (Figure 5D) and new O species (O-Ru_xO_y) in the O 1s XPS spectrum (Figure 7D) of the same sample, it was important to determine the stoichiometry of the unknown ruthenium-oxygen compounds formed due to oxidation of sample C. Figure 11D was plotted to show the evolution of normalized intensity ratio between peaks labelled Ru_xO_y 5/2, Ru_xO_y 3/2, PL Ru_xO_y 5/2, PL Ru_xO_y 3/2 of Ru 3d spectrum (figure 5D) and peak O-Ru_xO_y of O 1s spectrum (figure 7D) during oxidation of sample C. From figure 11D, it was observable that the O/Ru ratio reaches an equilibrium value of 2.5 at the same time as the total amount of Ru-Ru_xO_y and O-Ru_xO_y species in Figure 10C saturated.

5. Discussion

5.1. Determination of silicide compounds

The Ru 3d peak positions observed in Figure 1A and Table 4, as demonstrated in previous studies [6] correspond to the presence of metallic Ru on the sample's surface. Therefore, confirming the material deposited on the Si (100) substrate was indeed metallic Ru.

The disappearance of asymmetry in the Ru 3d peaks in Figure 1C and the appearance of a new Si peak in Figure 1D, in agreement with previous studies [2,7], gave the first confirmation that ruthenium silicide compounds formed at the surface of the samples after each sample was UHV annealed at 700 C for at least 80 minutes. Additionally, the Ru 3d and Si 2p peak position observed in Figures 1C and 1D respectively, in good agreement with previous XPS studies, also indicate the formation of ruthenium silicide compounds at the surface of the samples [2,17]. The second confirmation for the presence of ruthenium silicide compounds at the surface of samples A, B, and C was indicated by Figures 2A, 2B, and 2C respectively. Here, it was observed that during annealing of the pristine samples, the atomic concentration of Ru species at the sample's surface decreased to 40% in sample A, 38% in sample B and 52% in sample C. While the atomic concentration of Si species at the sample's surface increased to 60% in samples A, and B, and 48% in sample C. These observations indicate that the silicon atoms diffused through the PLD-deposited Ru during the annealing process to form ruthenium silicide compounds. This argument is supported by previous observations that showed that ruthenium silicide formation during annealing happens because of the kinetic diffusion of silicon atoms and the ruthenium atoms toward the surface to form ruthenium silicide compounds at the surface of the sample [1].

To study the oxidation of ruthenium silicide compounds it was important to confirm the stoichiometric ratio of ruthenium silicide compounds formed at the surface of the samples during the annealing process. The first confirmation of the stoichiometric ratio of the ruthenium silicide compounds formed at the surface was provided by the Si/Ru ratios observed in Figure 3A. From this figure, it was observed that the 1.6 ratio detected for sample B indicates the formation of Ru_2Si_3 compound at the surface of this sample. Similarly, for sample A, the 1.4 ratio detected indicates the formation of Ru_2Si_3 and a mix of other silicide compounds at the sample's surface. Finally, in the case of sample C, the 0.9 Si/Ru ratio indicates the possibility that the RuSi compound was formed at the surface of this sample instead of the expected Ru_2Si_3.

To confirm that the Si/Ru ratios of samples A and C observed in Figure 3A indicate the speculated ruthenium silicide compounds, Figures 4B and 4C were plotted to show the after-annealing high-resolution extended Ru 3d XPS spectra. A previous study on the plasmon loss peak positions observed in the extended Ru 3d XPS spectra have shown that the plasmon loss peak position and shape changes when the stoichiometric ratio of the ruthenium-based compounds present at the surface of the sample changes [2]. According to S. van Vliet *et al.*, the PL peak positions observed for sample A in Figure 4B at +22.5 eV and +26.7eV away from the $Ru3d_{5/2}$ peak position correspond to the formation of Ru_2Si_3 + RuSi compounds at the sample's surface. The same study also showed that the PL peaks for sample C observed at

+23.5 eV and +27.7 eV away from the Ru $3d_{5/2}$ peak position in Figure 4C, corresponds to the formation of RuSi compound at the surface of the sample.

The formation of different silicide compounds during the UHV annealing of the samples was an unexpected result. The first possible explanation for the difference in the formation of silicide compounds could be attributed to the PLD method that was used to deposit metallic Ru on top of the Si (100) substrate. The only difference between depositions of each sample was that samples A and B were created with a laser fluence of 8.1 J/cm^2, while sample C was created with a laser fluence of 8.3 J/cm^2. However, it is highly unlikely that the energy difference of 0.2 J/cm^2 in the laser fluence during the deposition of Ru on Si (100) would result in deposition of ruthenium with a different energy on the Si (100) substrate. Thus, the PLD method is not attributed to the formation of different silicides.

The second possible source for the formation of different ruthenium silicide compounds could be the annealing temperature. However, during the annealing process, all samples were kept at a constant temperature of 700°C for at least 80 minutes to enable complete silicide formation, and the surface temperature was recorded at regular intervals using an infrared pyrometer. The pyrometer that is used to record the sample temperatures has an error of ±2.1°C [8]. However, this should not make a difference in silicide formation since previous studies [1, 2, 9] have shown that when a sample with metallic Ru thin film deposited on top of a Si (100) is annealed at 625°C for 60 minutes, only Ru_2Si_3 phase is observable [1, 2, 9]. The study also indicates that if there is enough silicon present, Ru_2Si_3 formation should happen during the annealing of the sample at any temperature above 625°C [1].

The third possible source of variation would be the Si (100) substrate. All samples were prepared using the same procedure described in the Method section and the silicon substrates with native silicon oxide layer used for the experiments are from the same Si (100) disk, thereby eliminating the Methods used for preparing the samples as a possible source of contamination.

The fourth possible reason for the silicide formation discrepancy between samples A and C could be the depletion of the silicon layer during the annealing of the sample [3]. However, to confirm that the compounds that have been determined using the Si/Ru ratio and plasmon-loss satellites/peak position are more or less accurate additional data from the x-ray diffraction technique (XRD) is needed. Using XRD it can be confirmed if the Ru_2Si_3 orthorhombic phase is present in samples A and B. XRD can also be used to confirm if the RuSi CsCl-type structure or FeSi-type structure is formed partially in sample A and completely in sample C.

Although the formation of RuSi phase in case of sample C was an unexpected result, past literature [18, 19] on the thermodynamic assessment of the Ru-Si have shown that the enthalpy of formation of the Ru2Si3 phase and the RuSi phase only differs by 6 kJ mol^{-1}. According to L. Perring *et al.,* if the atomic percentage of Si is less than 60%, the formation of RuSi phase or Ru_2Si_3 phase or both together (like in sample A) can occur during the annealing process [19].

An additional peak, named NUP was discovered to appear In the after-annealing Ru 3d XPS spectra in Figure 1C. Subsequently, from figures 2A, 2B, and 2C it was confirmed that the

NUP is present in all samples after they were annealed. It was also observed that the saturation point for the increase in atomic concentration of NUP was very close to the saturation point for the decrease in atomic concentration of total Ru species. To confirm that the NUP contributes to determining the correct Si/Ru ratios, the observed Si/Ru ratio for all three samples with and without the NUP was plotted in Figure 3B. The Si/Ru ratios calculated including NUP coincide with previously observed Si/Ru ratios plotted in 3A, where it was assumed that NUP is a peak indicating a new Ru species. The Si/Ru ratios, observed in Figure 3B, show that the Si/Ru ratios excluding NUP were not equal to the expected Si/Ru ratio for all samples. The above observations support the argument that the NUP is a real peak. However, the Ru species that this peak indicates is still unidentified because the spin-orbit coupling characteristics of Ru 3d orbital in XPS indicate that another NUP should exist at ±4.17 eV (spin-orbit coupling split distance between Ru $3d_{5/2}$ and Ru $3d_{3/2}$ peak positions) from the current identified NUP position (Figure 1C) but that observation was not made. Thereby indicating that the NUP might not be a new Ru species.

The second possible explanation for the presence of the NUP could be the presence of carbon-based compounds at the surface of the samples. This is because XPS is a core-level spectroscopy technique, and because of this feature of XPS the BE of Ru 3d core–levels superimpose the BE of C 1s core–levels [4, 20]. This is the most likely explanation for the presence of NUP is all of the samples. Although it still does not completely explain why the Si/Ru ratios observed including the NUP would be more accurate than the Si/Ru ratio excluding NUP. The increase Si/Ru ratios excluding NUP could be attributed to the enrichment of the surface with increasing Si atoms. Therefore, additional research on ruthenium silicide compounds is needed to determine whether the NUP indicates a different ruthenium species or a carbon-based compound that reacts with Ru or Si.

5.2. Analyzing oxidation of ruthenium silicide compounds

Since the post-annealing high-resolution extended Ru 3d spectrum for sample B was not recorded due to a random error, therefore the post-oxidation high-resolution extended Ru 3d XPS spectra for sample B in Figure 8C was used to determine the stoichiometry of the ruthenium silicide compounds formed at the sample B's surface. According to a previous study [2], the PL peak positions observed in Figure 8C indicate the presence of Ru_2Si_3 compound. The above result along with the observed Si/Ru ratio of 1.6 for sample B gives confirmation that annealing of sample B resulted in the formation of Ru_2Si_3 compound at the sample's surface.

As mentioned in the results section, observations from the post-oxidation Ru 3d XPS spectra of samples A (figure 5B) and B (figure 5C) showed that the peak shape and position of the Ru 3d peaks observed in Figures 5B and 5C, remained unchanged after oxidation of both the samples. In agreement with previous studies [10, 11, 12], this was the first result proving that the Ru in Ru_2Si_3+RuSi (sample A) and Ru_2Si_3 (sample B) present at the surface of the samples do not oxidize to form ruthenium-based oxides at the temperatures and pressures mentioned in Table 3. In the case of sample A, the abscene of oxidation of Ru in Ru_2Si_3+ RuSi was also supported by Figure 8B where it was observed that the post-oxidation high-resolution extended Ru 3d XPS spectra for this sample remained unchanged after oxidation. Although it was not possible to determine in the case of sample B whether the post-annealing high-resolution extended Ru 3d XPS spectra was different from the post-oxidation high-resolution extended Ru 3d spectra observed in Figure 8C in terms of peak shape and plasmon-loss peak position. It was observed from Figure 5C that, after oxidation of sample B no additional peaks were detected in the post-oxidation Ru 3d XPS spectra. This observation in agreement with previous literature [10, 11, 12] indicates that the Ru in Ru_2Si_3 did not oxidize at the conditions mentioned in Table 3. The above-mentioned observations were also supported by Figure 11C, where it was observed that the post-oxidation Si/Ru ratios for samples A, and B remained unchanged and were equal to the post-annealing Si/Ru ratios observed in Figure 3A for samples A, and B. Thus, from the observations made so far, it is concluded that the Ru in Ru_2Si_3+RuSi (oxidized at 350°C)and Ru_2Si_3 (oxidized at 700°C) does not oxidize at any oxygen pressure mentioned in Table 3.

The observed linear increase in the total amount of Si_xO_y species and O-Si species until a certain time and the linear decrease in the total amount of Si-Ru_xSi_y species until a certain time in Figure 10A gave the first indication that new species formed at the surface of sample A. Since it was shown above that the ruthenium is ruthenium silicide compounds observed in sample A did not oxidize to form a new ruthenium-based compound at the surface, the only remaining element that oxygen could oxidize is silicon. Thus, the second proof for the formation of a Si_xO_y compound at sample A's surface was provided by the after-oxidation Si 2p and O 1s XPS spectra in Figures 6B and 7B respectively. From Figures 6B and 7B, the presence of new Si and O species at the surface of the sample was observable. The peak position of Si– Si_xO_y –3/2 peak at 102.2 eV and Si– Si_xO_y –1/2 peak at 102.8 eV observed in Figure 6B indicate the formation of Si_xO_y compounds at the sample's surface. Due to the location of the Si_xO_y peaks in the Si 2p XPS spectra, it was determined that these two peaks do not indicate different silicon-oxide compounds and instead emerge from the spin-orbit

coupling split of the Si 2p orbital that is known to happen in the Si 2p XPS spectra. Thus, the Si–Si_xO_y – 3/2 peak corresponds to the Si 2p3/2 orbital, and the Si–Si_xO_y–1/2 peak corresponds to the Si 2p1/2 orbital. Previous XPS studies have not mentioned the observed this spin-orbit coupling split in the peak indicating the formation of Si_xO_y compounds in the Si 2p XPS spectra. However, previous XPS studies [10,11, 12] on the oxidation of ruthenium silicide compounds on a Si (100) substrate at similar temperatures and pressures have shown that thermal oxidation of ruthenium silicide compounds results in the formation of SiO_2 compound at a sample's surface. According to the mentioned studies the formation of SiO_2 results in a new peak at 102.4eV in the Si 2p XPS spectra. It is important to mention that the spin-orbit coupling split of the peak indicating Si_xO_y compound formation in the Si 2p XPS spectra was observed in the case of all samples (Figures 6B-6D).

According to previous literature [13, 14], additional confirmation on the formation of silicon oxide compounds at the sample's surface can be and was, confirmed by the emergence of an O-Si_xO_y peak at 531.7eV in the O 1s spectra shown in figure 7B. This was an expected result, since previous studies on the oxidation of metal silicide compounds, have shown that oxidizing metal silicide compounds at 350°C results in the formation of Si_xO_y compounds at the sample's surface, and the most likely candidate is the SiO_2 species [1, 10, 11, 12]. The formation of Si_xO_y on the sample's surface is supported by previous studies where it was shown that it is thermodynamically favorable for Si atoms to diffuse through the ruthenium silicide layer to form silicon oxide compounds at the sample's surface [1, 10]. To confirm SiO_2 compound formation at the surface of sample A, the O/Si ratio of sample A was plotted in Figure 11B. From Figure 11B, it was observed that the O/Si ratio for Sample A grew linearly until the 235-minute mark and then saturated at an O/Si ratio of 2.1. Thereby confirming that the SiO_2 compound was formed at the surface of sample A.

Although it was determined from the annealing experiments that the ruthenium silicide compounds formed at the surface of the samples during annealing of the pristine samples A and B were different, it was shown above that the ruthenium in ruthenium silicide compounds at sample B's surface also did not oxidize to form ruthenium-oxide compounds. Therefore, the oxidation of sample B, like that of sample A, resulted in the formation of Si_xO_y compounds at the surface of sample B. Like sample A, the after-oxidation Si 2p XPS and O 1s spectra of sample B, observed in figures 6C, and 7C respectively, indicated the presence of new Si and O species. From Figure 6C, it was determined that, like in the case of sample A above, the Si–Si_xO_y –3/2 and the Si–Si_xO_y –½2 peak positions indicate the presence of silicon-oxide compounds at the surface [1, 10, 11, 12]. From Figure 11B, it was also observed that the O/Si ratio for Sample B grew linearly up to the 150–minute mark after which the O/Si ratio stabilized at a value of 2.5. Thereby indicating that the oxidation of sample B resulted in the formation of the Si_2O_5 compound instead of the expected SiO_2. Although the formation of Si_2O_5 is an unexpected result, a previous study on ultra-thin silica films on metals has shown that at high temperatures and pressures the formation of Si_2O_5 adlayer is favored over the formation of SiO_2 because of the abundance of Si in an oxygen-rich environment [15]. However, it is highly unlikely that Si gave up 5 electrons to end in the +5 oxidation state. Thus it is suspected that the 2.5 ratio observed for this sample maybe because of enrichment of oxygen at the sampls's surface which cause the an increased O/Si ratio for sample B.

The above results show that the oxidation of ruthenium silicide compounds in samples A and B did not oxidize ruthenium in Ru_2Si_3+ RuSi and Ru_2Si_3 respectively and instead preferred to form silicon oxide compounds at the surface of the samples with different stoichiometric ratios. From Figure 11A, it was also observed that the oxidation percentage for sample A was 14.6%, and that of sample B was 52.1%. Observations from Figures 10A, 10B, and 11A also show that the growth in the amount of oxygen species and the growth in the oxidation ratio have the saturation point in the case of samples A, and B. Since the only difference between the oxidation of the two samples was the temperature at which the two samples were oxidized, it leads to agreement with previous studies [1, 10, 11, 12] that the oxidation of ruthenium silicide compounds and the subsequent formation of silicon-oxide compounds at the surface of samples A, and B is temperature-dependent. Thereby supporting observations from previous studies that showed that oxidation of a thin-film of Ru_2Si_3 on top of Si (100) substrate, results in the formation of silicon-oxide compounds at the surface of the samples. Additionally, the studies [1, 10, 11, 12, 15] also show that the stoichiometry of Si_xO_y compounds, the oxidation percentage, and the amount of silicon oxide compounds formed at the surface of samples A, and B, are dependent on the temperature at which the samples were oxidized.

Observations from Figures 5D and 7D showed that the oxidation of the RuSi compound in sample C resulted in the formation of new ruthenium and oxygen species at the sample's surface. As reported in previous literature [4], and observed in Figure 5D and Table 4, the new peaks and their peak positions that emerged in the Ru 3d XPS spectra (figure 5D) correspond to the formation of ruthenium oxide compounds ($Ru–Ru_xO_y$ – 5/2 and $Ru–Ru_xO_y$ – 3/2) and the plasmon-loss satellites (PL Ru_xO_y – 5/2 and PL Ru_xO_y – 3/2) associated with the formation of ruthenium oxide compounds. Similarly, previous studies [4, 13] also show that one of the new peaks emerging in O 1s spectra in Figure 7D ($O–Ru_xO_y$) also corresponds to the formation of Ru_xO_y compounds at the sample's surface. The formation of RuO_2 at the surface of sample C was also confirmed using the O/Ru ratio plotted in Figure 11D, from where it was observable that at the 165–minute mark, the O/Ru ratio saturates with a value of 2.1, thereby confirming the formation of RuO_2 compound at the surface of sample C. This was an unexpected result since previous studies on the oxidation of ruthenium silicide compounds have not provided any evidence that ruthenium in RuSi compound oxidizes at 550°C and oxygen pressures displayed in Table 3 [1, 10, 11, 12].

Like sample A, previous literature [13, 14] have shown that the position (Table 4) of the new peaks that emerged in the Si 2p XPS spectra (Si_xO_y 3/2 and Si_xO_y 1/2) and O 1s XPS spectra (O–Si) shown in figures 6D and 7D respectively indicate the formation of the SiO_2 species at the surface of sample C. The confirmation of SiO_2 at the sample's surface was also provided by Figure 11B, where it was observed that the O/Si ratio for sample C, saturates at a value of 2.1, thereby confirming the formation of SiO_2 compound. From Figure 11C, it was also revealed that the oxidation of RuSi causes the Si/Ru ratio of sample C to increase from 0.9 to 1.2. The slight increase in the Si/Ru ratio of sample C did not affect the stoichiometry of the RuSi compound significantly because from Figure 8D it was determined that the position of the PL peaks remained unchanged after oxidation of sample C. This result was also

unexpected since previous studies have not shown the oxidation of ruthenium in ruthenium silicide compounds, and therefore not shown how the oxidation of ruthenium affects the original ruthenium silicide compounds formed during annealing of the samples. However, as mentioned above, it is highly unlikely that the stoichiometry of the ruthenium silicide compounds changed after the oxidation of sample C since the position of plasmon-loss peaks after oxidation still corresponds to the formation of the RuSi compound [2]. It is also possible that during the UHV-annealing process of sample C, some PLD-deposited Ru did not react with Si to form ruthenium silicide compounds, and resulted in the formation of RuSi compound. Thereafter the thermal oxidation of sample C at 550°C caused the remaining metallic Ru to react with oxygen and Si again to form new ruthenium oxide compounds as well react with further Si to try and form Ru_2Si_3 compound. However, as mentioned in the above discussion for silicides, all the samples were UHV annealed for at least 80 minutes at 700°C to enable Ru_2Si_3 formation and the same is true for sample C, which was also UHV annealed for 90 minutes. Thereby eliminating the possibility that some of the metallic Ru was unable to react with Si to form ruthenium silicide compounds.

Sample Name	Figure Number	Peak	Position Observed (eV)
A	1A	Ru $3d_{5/2}$	279.7
C	5D	Ru–Ru_xSi_y	279.9
C	5D	Ru–Ru_xO_y – 5/2	280.5
C	5D	PL–Ru_xO_y – 5/2	281.9
C	6D	O– Si_xO_y	531.8
C	6D	O– Ru_xO_y	529.5
C	6D	O– adsorbed	528.9

Table 4: Observed peak positions of important peaks after oxidation of sample C.

Before moving to the conclusion, it is important to mention that according to previous studies [16, 21] the O-adsorbed peak, which was observed in Figures 7B, 7C, and 7D corresponds to the presence of O_2 gas that did not react with either ruthenium or silicon atoms. According to Y. Enta *et al*., during thermal oxidation of silicon oxide at temperatures up to 700°C, molecular oxygen has the tendency to adsorb and desorb from the silicon oxide surface. This behavior of adsorption and desorption of oxygen was also observable during thermal oxidation of all three samples and is clearly displayed in Figures 10A, 10B and 10C. Thus, the O-adsorbed peak is not used for calculating the O/Si ratio or the O/Ru ratio but was used for calculating the oxidation percentage in Figure 11A because adsorbed oxygen was present at the surface of all three samples. An additional goal of this study was to find whether the formation of $Ru_xSi_yO_w$ compound occurs between the ruthenium silicide layer and the silicon oxide layer. However, no indication of $Ru_xSi_yO_w$ compound formation was observed during any experiments since no additional peaks were observed in any spectra shown above, that would indicate the formation of a $Ru_xSi_yO_w$ compound at the sample's surface.

6. Conclusion

UHV annealing of PLD-deposited Ru on Si (100) substrate at 700°C for three different samples (A, B, and C) that were created using the same PLD–deposition parameters and the same materials as reported in this study may result in the formation of three different types of ruthenium silicide compounds namely Ru_2Si_3 + RuSi, Ru_2Si_3 and RuSi. UHV annealing of the three samples also resulted in the emergence of NUP, which was most likely be characterized as a C 1s peak, indicating the presence of 5-10% carbon contamination in the samples. Results from the oxidation of ruthenium silicide compounds, in agreement with previous studies, show that the Ru_2Si_3 phase and the combination of Ru_2Si_3 + RuSi phases do not oxidize Ru at any temperature and pressure mentioned in this study and only results in the formation of silicon oxide compounds. On the other hand, the oxidation of RuSi compound, observed in case of sample C, showed that the oxidation of the RuSi phase at 550°C causes the oxidation of ruthenium in RuSi and results in the formation of rutile ruthenium oxide and silicon oxide layer on top of the RuSi phase.

In conclusion, and in agreement with previous studies [10, 12], this research also shows that when the Ru_2Si_3 phase is the dominant silicide phase at a sample's surface, the oxidation of such a sample will only result in the formation of a Si_xO_y layer on top of the ruthenium silicide compounds and without affecting or changing the stoichiometric ratio of the ruthenium silicide compounds. The oxidation of ruthenium in the RuSi phase also caused the stoichiometric ratio of the RuSi compound to change, suggesting that the diffusion kinetics of ruthenium atoms, silicon atoms, and oxygen molecules, needs to be studied in more detail at different temperatures and oxygen pressures to determine what causes the oxidation of the RuSi phase. Finally, no evidence on the formation of a Ru-Si-O compound was evident from the XPS spectra.

Therefore, if ruthenium silicide compounds are to be utilized as oxidation resistant coatings or as an alternative for metallic Ru thin-films in semiconductor technology the oxidation of Ru_2Si_3 at 550°C needs to be studied to confirm that this silicide phase does not oxidize at this temperature, unlike the RuSi phase which was observed to oxidize at 550°C. Additionally, in-situ XPS oxidation studies on the RuSi phase are needed to determine if the RuSi phase oxidizes at the temperatures at which the Ru_2Si_3 phase did not oxidize.

7. References

7.1. Introduction

1. S.-L. Zhang and M. Östling, “Metal silicides in CMOS Technology: Past, present, and future trends,” Critical Reviews in Solid State and Materials Sciences, vol. 28, no. 1, pp. 1–129, Nov. 2003, doi: 10.1080/10408430390802431.
2. X. Duan and Y. Huang, “Chemically synthesized semiconductor nanowires for High-Performance electronics and optoelectronics,” in Elsevier eBooks, 2010, pp. 27–66. doi: 10.1016/b978-1-4377-7823-6.00002-7.
3. J. Hertel, C. Schwinge, L. Gerlich, and M. Wagner-Reetz, “300 mm CMOS-compatible fabrication of Ru2Si3 sub-50 nm thin films and characterization,” Applied Physics Letters, vol. 120, no. 22, May 2022, doi: 10.1063/5.0080245.
4. I. Melngailis, “Small bandgap semiconductor infrared detectors,” Journal of Luminescence, vol. 7, pp. 501–523, Jan. 1973, doi: 10.1016/0022-2313(73)90081-1.
5. D. Souptel, G. Behr, L. Ivanenko, H. Vinzelberg, and J. Schumann, “Floating zone growth and characterization of semiconducting Ru2Si3 single crystals,” Journal of Crystal Growth, vol. 244, no. 3–4, pp. 296–304, Oct. 2002, doi: 10.1016/s0022-0248(02)01686-x.
6. K. Shudo, S. Ohno, M. Toramaru, N. Kobayashi, Y. Miyamoto, and N. Kawamura, “Microstructure and local density of states of ruthenium silicide on SI(001) surface,” Materials Transactions, vol. 53, no. 9, pp. 1582–1585, Jan. 2012, doi: 10.2320/matertrans.m2012154.
7. D. Lenssen et al., “Growth and structural characterization of semiconducting Ru2Si3,” Journal of Luminescence, vol. 80, no. 1–4, pp. 461–465, Dec. 1998, doi: 10.1016/s0022-2313(98)00148-3.
8. A. Basu, R. P. Hennessy, G. G. Adams, and N. E. McGruer, “Hot switching damage mechanisms in MEMS contacts—evidence and understanding,” Journal of Micromechanics and Microengineering, vol. 24, no. 10, p. 105004, Sep. 2014, doi: 10.1088/0960-1317/24/10/105004.
9. E. A. Смирнова, A. V. Miakonkikh, A. E. Rogozhin, and K. B. Руденко, “Atomic layer deposition of Ruthenium on different interfaces for an advanced metallization system of ICs,” Journal of Physics: Conference Series, vol. 1695, no. 1, p. 012045, Dec. 2020, doi: 10.1088/1742-6596/1695/1/012045.
10. J. Gebhardt and D. F. Urban, “Influence of Impurity Atoms on Hydrogen Diffusion into Ruthenium,” Journal of Physical Chemistry. C, vol. 126, no. 46, pp. 19895–19903, Nov. 2022, doi: 10.1021/acs.jpcc.2c05840.
11. B. A. Banks, S. K. Miller, K. K. deGroh, and R. Demko, “Atomic Oxygen Effects on Spacecraft Materials,” NASA, Jun. 2003, [Online]. Available: https://ntrs.nasa.gov/api/citations/20030062195/downloads/20030062195.pdf
12. C. S. Petersson, J. E. E. Baglin, J. Dempsey, F. M. D’Heurle, and S. J. La Placa, “Silicides of ruthenium and osmium: Thin film reactions, diffusion, nucleation, and stability,” Journal of Applied Physics, vol. 53, no. 7, pp. 4866–4883, Jul. 1982, doi: 10.1063/1.331319.
13. S. Van Vliet, A. Troglia, E. Olsson, and R. Bliem, “Identifying silicides via plasmon loss satellites in photoemission of the Ru-Si system,” Applied Surface Science, vol. 608, p. 155139, Jan. 2023, doi: 10.1016/j.apsusc.2022.155139.

14. Y. He et al., “Discovery and facile synthesis of a new silicon based family as efficient hydrogen evolution reaction catalysts: A computational and experimental investigation of metal monosilicides,” Small (Weinheim. Print), vol. 17, no. 8, Jan. 2021, doi: 10.1002/smll.202006153.
15. T. Tsarfati, E. Zoethout, R. W. E. Van De Kruijs, and F. Bijkerk, “Growth and sacrificial oxidation of transition metal nanolayers,” Surface Science, vol. 603, no. 7, pp. 1041–1045, Apr. 2009, doi: 10.1016/j.susc.2009.02.027.
16. H. Y. H. Chan, C. G. Takoudis, and M. J. Weaver, “High-Pressure oxidation of ruthenium as probed by Surface-Enhanced RAMAN and X-Ray photoelectron spectroscopies,” Journal of Catalysis, vol. 172, no. 2, pp. 336–345, Dec. 1997, doi: 10.1006/jcat.1997.1841.
17. P. Osiceanu, “An XPS study on ion beam induced oxidation of titanium silicide,” Applied Surface Science (Print), vol. 253, no. 1, pp. 381–384, Oct. 2006, doi: 10.1016/j.apsusc.2006.06.018.
18. L. Perring, F. Bussy, J. C. Gachon, and P. Feschotte, “The Ruthenium–Silicon system,” Journal of Alloys and Compounds, vol. 284, no. 1–2, pp. 198–205, Mar. 1999, doi: 10.1016/s0925-8388(98)00911-6.
19. S. Lizzit et al., “Transfer-Free Electrical Insulation of Epitaxial Graphene from its Metal Substrate,” Nano Letters, vol. 12, no. 9, pp. 4503–4507, Aug. 2012, doi: 10.1021/nl301614j.

7.2. Theoretical background

7.2.1. Oxidation of ruthenium silicide

1. “NCI Dictionary of Cancer Terms,” Cancer.gov. https://www.cancer.gov/publications/dictionaries/cancer-terms/def/oxidation.
2. C. S. Petersson, J. E. E. Baglin, J. Dempsey, F. M. D’Heurle, and S. J. La Placa, “Silicides of ruthenium and osmium: Thin film reactions, diffusion, nucleation, and stability,” Journal of Applied Physics, vol. 53, no. 7, pp. 4866–4883, Jul. 1982, doi: 10.1063/1.331319.
3. F. M. D’Heurle, A. Cros, R. D. Frampton, and E. A. Irene, “Thermal oxidation of silicides on silicon,” Philosophical Magazine B-physics of Condensed Matter Statistical Mechanics Electronic Optical and Magnetic Properties, vol. 55, no. 2, pp. 291–308, Jan. 1987, doi: 10.1080/13642818708211210.
4. D. Lenssen et al., “Growth and structural characterization of semiconducting Ru2Si3,” Journal of Luminescence, vol. 80, no. 1–4, pp. 461–465, Dec. 1998, doi: 10.1016/s0022-2313(98)00148-3.
5. L. Pasquali, N. Mahne, M. Montecchi, V. Mattarello, and S. Nannarone, “Formation and distribution of compounds at the Ru–Si(001) ultrathin film interface,” Journal of Applied Physics, vol. 105, no. 4, Feb. 2009, doi: 10.1063/1.3079507.
6. S. Lizzit et al., “Transfer-Free Electrical Insulation of Epitaxial Graphene from its Metal Substrate,” Nano Letters, vol. 12, no. 9, pp. 4503–4507, Aug. 2012, doi: 10.1021/nl301614j.
7. J. T. Diulus, B. Tobler, J. Osterwalder, and Z. Novotný, “Thermal oxidation of Ru(0001) to RuO_2(110) studied with ambient pressure x-ray photoelectron

spectroscopy," Journal of Physics. D, Applied Physics (Print), vol. 54, no. 24, p. 244001, Mar. 2021, doi: 10.1088/1361-6463/abedfd.
8. S. Gupta et al., "Study of oxidation behaviour of Ruthenium thin film after thermal annealing in oxygen environment," Thin Solid Films, vol. 764, p. 139606, Jan. 2023, doi: 10.1016/j.tsf.2022.139606.
9. H. Shimizu and T. Sato, "Kinetics of ultrathin thermal oxide growth on SI(001) surfaces," Japanese Journal of Applied Physics, vol. 44, no. 2R, p. 808, Feb. 2005, doi: 10.1143/jjap.44.808.
10. Y. Matsui, Y. Nakamura, Y. Shimamoto, and M. Hiratani, "An oxidation barrier layer for metal–insulator–metal capacitors: ruthenium silicide," Thin Solid Films, vol. 437, no. 1–2, pp. 51–56, Aug. 2003, doi: 10.1016/s0040-6090(03)00606-0.

7.2.2. XPS

1. F. A. Stevie and C. L. Donley, "Introduction to x-ray photoelectron spectroscopy," Journal of Vacuum Science & Technology, vol. 38, no. 6, Sep. 2020, doi: 10.1116/6.0000412.
2. K. Oura, M. Katayama, A. B. Зотов, V. G. Lifshits, and A. A. Саранин, Surface science. 2003. doi: 10.1007/978-3-662-05179-5.
3. C. Mahuvava and F. C. P. Du Plessis, "Monte Carlo evaluation of the dose perturbation effect of hip prostheses for megavoltage photon radiotherapy," Physica Medica, vol. 31, p. S7, Sep. 2015, doi: 10.1016/j.ejmp.2015.07.108.
4. C. Sousa, T. Minerva, G. Pacchioni, P. S. Bagus, and F. Parmigiani, "Electrostatic and chemical bonding contributions to the cation core level binding energy shifts in MgO, CaO, SrO, BaO. A cluster model study," Journal of Electron Spectroscopy and Related Phenomena, vol. 63, no. 3, pp. 189–205, Oct. 1993, doi: 10.1016/0368-2048(93)87003-i.
5. D. R. Baer et al., "XPS guide: Charge neutralization and binding energy referencing for insulating samples," Journal of Vacuum Science & Technology. A. Vacuum, Surfaces, and Films, vol. 38, no. 3, Apr. 2020, doi: 10.1116/6.0000057.
6. P. Van Der Heide, X-ray Photoelectron Spectroscopy: An introduction to Principles and Practices. 2011. [Online]. Available: http://ci.nii.ac.jp/ncid/BB08062443.

7.3. Experimental Methods

1. S. Prabhu, D. K. Naveen, S. Bangera, and B. S. Bhat, "Production of X-RAYS using X-RAY Tube," Journal of Physics: Conference Series, vol. 1712, no. 1, p. 012036, Dec. 2020, doi: 10.1088/1742-6596/1712/1/012036.
2. "Inconel® 625," www.haraldpihl.com. https://www.haraldpihl.com/nl/producten/nikkellegeringen/inconel-625/
3. K. Oura, M. Katayama, A. B. Зотов, V. G. Lifshits, and A. A. Саранин, Surface science. 2003. doi: 10.1007/978-3-662-05179-5.
4. L.-Å. Näslund, A. S. Ingason, S. Holmin, and J. Rosén, "Formation of RUO(OH)2 on RUO2-Based electrodes for hydrogen production," The Journal of Physical Chemistry C, vol. 118, no. 28, pp. 15315–15323, Jul. 2014, doi: 10.1021/jp503960q.
5. S. Van Vliet, A. Troglia, E. Olsson, and R. Bliem, "Identifying silicides via plasmon loss satellites in photoemission of the Ru-Si system," Applied Surface Science, vol. 608, p. 155139, Jan. 2023, doi: 10.1016/j.apsusc.2022.155139.
6. H. Y. H. Chan, C. G. Takoudis, and M. J. Weaver, "High-Pressure oxidation of ruthenium as probed by Surface-Enhanced RAMAN and X-Ray photoelectron

spectroscopies," Journal of Catalysis, vol. 172, no. 2, pp. 336–345, Dec. 1997, doi: 10.1006/jcat.1997.1841.
7. F. M. D'Heurle, R. D. Frampton, E. A. Irene, H. Jiang, and C. S. Petersson, "Rate of formation of silicon dioxide; semiconducting ruthenium silicide," Applied Physics Letters, vol. 47, no. 11, pp. 1170–1172, Dec. 1985, doi: 10.1063/1.96315.
8. S. Lizzit et al., "Transfer-Free Electrical Insulation of Epitaxial Graphene from its Metal Substrate," Nano Letters, vol. 12, no. 9, pp. 4503–4507, Aug. 2012, doi: 10.1021/nl301614j.
9. J. F. Moulder, J. Chastain, and R. C. King, Handbook of x-ray photoelectron spectroscopy : a reference book of standard spectra for identification and interpretation of XPS data. 1995. [Online]. Available: http://ci.nii.ac.jp/ncid/BA30894637.
10. Z. Liu, "Laser applied coatings," in Elsevier eBooks, 2010, pp. 2622–2635. doi: 10.1016/b978-044452787-5.00141-4.

7.4. Results, Discussion and Conclusion

1. C. S. Petersson, J. E. E. Baglin, J. Dempsey, F. M. D'Heurle, and S. J. La Placa, "Silicides of ruthenium and osmium: Thin film reactions, diffusion, nucleation, and stability," Journal of Applied Physics, vol. 53, no. 7, pp. 4866–4883, Jul. 1982, doi: 10.1063/1.331319.
2. S. Van Vliet, A. Troglia, E. Olsson, and R. Bliem, "Identifying silicides via plasmon loss satellites in photoemission of the Ru-Si system," Applied Surface Science, vol. 608, p. 155139, Jan. 2023, doi: 10.1016/j.apsusc.2022.155139.
3. F. A. Stevie and C. L. Donley, "Introduction to x-ray photoelectron spectroscopy," Journal of Vacuum Science & Technology, vol. 38, no. 6, Sep. 2020, doi: 10.1116/6.0000412.
4. D. Morgan, "Resolving ruthenium: XPS studies of common ruthenium materials," Surface and Interface Analysis, vol. 47, no. 11, pp. 1072–1079, Sep. 2015, doi: 10.1002/sia.5852.
5. J. C. Kim, J. Ji, J. S. Kline, J. R. Tucker, and T. C. Shen, "Preparation of atomically clean and flat Si(1 0 0) surfaces by low-energy ion sputtering and low-temperature annealing," Applied Surface Science, vol. 220, no. 1–4, pp. 293–297, Dec. 2003, doi: 10.1016/s0169-4332(03)00826-2.
6. NIST X-ray Photoelectron Spectroscopy Database, NIST Standard Reference Database Number 20, National Institute of Standards and Technology, Gaithersburg MD, 20899 (2000), DOI: https://dx.doi.org/10.18434/T4T88K, (retrieved [Mar. 2024]).
7. H. Chen et al., "Promoting Subordinate, Efficient Ruthenium Sites with Interstitial Silicon for Pt-Like Electrocatalytic Activity," Angewandte Chemie, vol. 131, no. 33, pp. 11531–11535, Jul. 2019, doi: 10.1002/ange.201906394.
8. Sensortherm GmbH, "METIS M311 (2-Color Pyrometer) - SensorTherm," Sensortherm, Sep. 21, 2023. https://www.sensortherm.de/en/product/metis-m311-2-color-pyrometer/
9. Troglia et al., "Free-standing nanolayers based on Ru silicide formation on Si(100)," Physical Review Materials, vol. 6, no. 4, Apr. 2022, doi: 10.1103/physrevmaterials.6.043402.

10. F. M. D'Heurle, R. D. Frampton, E. A. Irene, H. Jiang, and C. S. Petersson, "Rate of formation of silicon dioxide; semiconducting ruthenium silicide," Applied Physics Letters, vol. 47, no. 11, pp. 1170–1172, Dec. 1985, doi: 10.1063/1.96315.
11. Y. Matsui, Y. Nakamura, Y. Shimamoto, and M. Hiratani, "An oxidation barrier layer for metal–insulator–metal capacitors: ruthenium silicide," Thin Solid Films, vol. 437, no. 1–2, pp. 51–56, Aug. 2003, doi: 10.1016/s0040-6090(03)00606-0.
12. S. Lizzit et al., "Transfer-Free Electrical Insulation of Epitaxial Graphene from its Metal Substrate," Nano Letters, vol. 12, no. 9, pp. 4503–4507, Aug. 2012, doi: 10.1021/nl301614j.
13. J. F. Moulder, J. Chastain, and R. C. King, Handbook of x-ray photoelectron spectroscopy : a reference book of standard spectra for identification and interpretation of XPS data. 1995. [Online]. Available: http://ci.nii.ac.jp/ncid/BA30894637.
14. D. S. Jensen et al., "Silicon (100)/SIO2 by XPS," Surface Science Spectra, vol. 20, no. 1, pp. 36–42, Sep. 2013, doi: 10.1116/11.20121101.
15. S. K. Shaikhutdinov and H. Freund, "Ultrathin silica films on metals: the long and winding road to understanding the atomic structure," Advanced Materials, vol. 25, no. 1, pp. 49–67, Nov. 2012, doi: 10.1002/adma.201203426.
16. H. Y. H. Chan, C. G. Takoudis, and M. J. Weaver, "High-Pressure oxidation of ruthenium as probed by Surface-Enhanced RAMAN and X-Ray photoelectron spectroscopies," Journal of Catalysis, vol. 172, no. 2, pp. 336–345, Dec. 1997, doi: 10.1006/jcat.1997.1841.
17. E. V. Jelenković, S. To, M. G. Blackford, O. Kutsay, and S. K. Jha, "XPS and TEM study of deposited and Ru–Si solid state reaction grown ruthenium silicides on silicon," Materials Science in Semiconductor Processing, vol. 40, pp. 817–821, Dec. 2015, doi: 10.1016/j.mssp.2015.07.085.
18. Y. Q. Liu, G. Shao, and K. P. Homewood, "Thermodynamic assessment of the Ru–Si and Os–Si systems," Journal of Alloys and Compounds, vol. 320, no. 1, pp. 72–79, May 2001, doi: 10.1016/s0925-8388(01)00931-8.
19. L. Perring, F. Bussy, J. C. Gachon, and P. Feschotte, "The Ruthenium–Silicon system," Journal of Alloys and Compounds, vol. 284, no. 1–2, pp. 198–205, Mar. 1999, doi: 10.1016/s0925-8388(98)00911-6.
20. J. Gómez-Bolívar et al., "Synthesis of Pd/Ru Bimetallic Nanoparticles by Escherichia coli and Potential as a Catalyst for Upgrading 5-Hydroxymethyl Furfural Into Liquid Fuel Precursors," Frontiers in Microbiology, vol. 10, Jun. 2019, doi: 10.3389/fmicb.2019.01276.
21. Y. Enta, H. Nakazawa, S. Sato, H. Kato, and Y. Sakisaka, "Silicon thermal oxidation and its thermal desorption investigated by Si 2p core-level photoemission," Journal of Physics. Conference Series, vol. 235, p. 012008, Jun. 2010, doi: 10.1088/1742-6596/235/1/012008.